

# The global surface temperatures of the Moon as measured by the Diviner Lunar Radiometer Experiment



J.-P. Williams <sup>a,\*</sup>, D.A. Paige <sup>a</sup>, B.T. Greenhagen <sup>b</sup>, E. Sefton-Nash <sup>c</sup>

<sup>a</sup> Department Earth, Planetary and Space Sciences, University of California, Los Angeles, CA 90095, USA

<sup>b</sup> Johns Hopkins University, Applied Physics Laboratory, 11100 Johns Hopkins Road, Laurel, MD 20723, USA

<sup>c</sup> Department of Earth and Planetary Sciences, Birkbeck, University of London, Malet Street, London, WC1E 7HX, UK

## ARTICLE INFO

### Article history:

Received 12 August 2015

Revised 4 June 2016

Accepted 11 August 2016

Available online 13 August 2016

### Keywords:

Moon  
Surface  
Regolith  
Infrared observations  
Temperature  
Radiance  
Remote sensing

## ABSTRACT

The Diviner Lunar Radiometer Experiment onboard the Lunar Reconnaissance Orbiter (LRO) has been acquiring solar reflectance and mid-infrared radiance measurements nearly continuously since July of 2009. Diviner is providing the most comprehensive view of how regoliths on airless bodies store and exchange thermal energy with the space environment. Approximately a quarter trillion calibrated radiance measurements of the Moon, acquired over 5.5 years by Diviner, have been compiled into a  $0.5^\circ$  resolution global dataset with a 0.25 h local time resolution. Maps generated with this dataset provide a global perspective of the surface energy balance of the Moon and reveal the complex and extreme nature of the lunar surface thermal environment. Our achievable map resolution, both spatially and temporally, will continue to improve with further data acquisition.

Daytime maximum temperatures are sensitive to the albedo of the surface and are  $\sim 387$ – $397$  K at the equator, dropping to  $\sim 95$  K just before sunrise, though anomalously warm areas characterized by high rock abundances can be  $> 50$  K warmer than the zonal average nighttime temperatures. An asymmetry is observed between the morning and afternoon temperatures due to the thermal inertia of the lunar regolith with the dusk terminator  $\sim 30$  K warmer than the dawn terminator at the equator. An increase in albedo with incidence angle is required to explain the observed decrease in temperatures with latitude. At incidence angles exceeding  $\sim 40^\circ$ , topography and surface roughness influence temperatures resulting in increasing scatter in temperatures and anisothermality between Diviner channels.

Nighttime temperatures are sensitive to the thermophysical properties of the regolith. High thermal inertia (TI) materials such as large rocks, remain warmer during the long lunar night and result in anomalously warm nighttime temperatures and anisothermality in the Diviner channels. Anomalous maximum and minimum temperatures are highlighted by subtracting the zonal mean temperatures from maps. Terrains can be characterized as low or high reflectance and low or high TI. Low maximum temperatures result from high reflectance surfaces while low minimum temperatures from low-TI material. Conversely, high maximum temperatures result from dark surface, and high minimum temperatures from high-TI materials.

Impact craters are found to modify regolith properties over large distances. The thermal signature of Tycho is asymmetric, consistent with an oblique impact coming from the west. Some prominent crater rays are visible in the thermal data and require material with a higher thermal inertial than nominal regolith. The influence of the formation of the Orientale basin on the regolith properties is observable over a substantial portion of the western hemisphere despite its age ( $\sim 3.8$  Gyr), and may have contributed to mixing of highland and mare material on the southwest margin of Oceanus Procellarum where the gradient in radiative properties at the mare-highland contact is broad ( $\sim 200$  km).

© 2016 The Authors. Published by Elsevier Inc.  
This is an open access article under the CC BY-NC-ND license  
(<http://creativecommons.org/licenses/by-nc-nd/4.0/>).

## 1. Introduction

The Diviner Lunar Radiometer Experiment (Diviner; [Paige et al., 2010a](#)) is one of seven instruments aboard NASA's Lunar Recon-

\* Corresponding author. Fax: 310 825 2279.

E-mail addresses: [jpierre@mars.ucla.edu](mailto:jpierre@mars.ucla.edu) (J.-P. Williams), [dap@moon.ucla.edu](mailto:dap@moon.ucla.edu) (D.A. Paige), [benjamin.greenhagen@jhuapl.edu](mailto:benjamin.greenhagen@jhuapl.edu) (B.T. Greenhagen), [e.sefton-nash@uclmail.net](mailto:e.sefton-nash@uclmail.net) (E. Sefton-Nash).

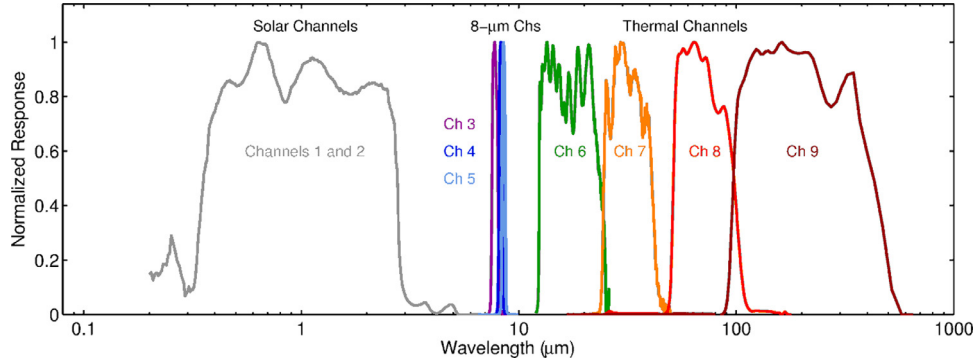


**Fig. 1.** Diviner's nine spectral passbands.

naissance Orbiter (LRO) (Chin et al., 2007; Tooley et al., 2010; Vondrak et al., 2010). Diviner has been systematically mapping the Moon since July 5, 2009 acquiring ~250 billion calibrated radiometric measurements (as of April 2015) at solar and infrared wavelengths covering a full range of latitudes, longitudes, local times and seasons. These are the first such comprehensive measurements of the Moon, or any other airless body, providing the ability to characterize the global lunar thermal environment, one of the most extreme of any planetary body in the solar system (Paige et al., 2010b).

The Moon is an important airless body to study not only because of its accessibility, but because it's ancient surface records events that occurred during the earliest phases of the formation of the Earth and the inner solar system. The Moon also exhibits a wide range of important planetary processes, such as impact cratering, volcanism, volatile cold-trapping and space weathering that relate directly to similar processes that are observed on both large and small bodies elsewhere in the solar system.

Early Diviner observations have been used to infer the average radiative and bulk thermophysical properties of the near-surface regolith at the equator (Vasavada et al., 2012). With continued operations, the current density of Diviner observations both spatially and in local time is high enough that diurnal temperatures can be adequately resolved globally at  $0.5 \text{ deg pix}^{-1}$  spatial resolution to create global gridded map datasets. This provides insight into the radiative and thermophysical properties of the lunar regolith globally. In this paper, we present an empirical view of the Moon as seen from Diviner, utilizing all acquired nadir-pointing observations without the aid of detailed physical models or laboratory data. We first discuss the Diviner instrument and its mapping history followed by the description of the data gridding and map production. We next present the maps in global, cylindrical projection and discuss and characterize the lunar global temperatures. This is followed by a discussion of processes that have resulted in widespread regolith modification that influence surface temperatures as observed by Diviner.

## 2. The diviner instrument

### 2.1. Instrument description

Diviner is a 9-channel radiometer that maps solar reflectance and infrared emission over a wavelength range of 0.3 to 400  $\mu\text{m}$  (Paige et al., 2010a). The spectral response of Diviner's channels is shown in Fig. 1. Channels 1 and 2, with identical spectral passbands of 0.35–2.8  $\mu\text{m}$ , measure reflected solar radiation from the lunar surface at two different sensitivities. The remaining channels (3–9) observe emitted infrared radiation from which brightness temperatures of the lunar surface are derived. The three narrow spectral passbands of channels 3–5 are used

to map the wavelength of the mid-infrared thermal emission maximum, a spectral feature called the Christiansen Feature (CF) near 8  $\mu\text{m}$  (Conel, 1996) which is diagnostic of the bulk silicate mineralogy (e.g. Greenhagen et al., 2010; Glotch et al., 2010, 2011). The remaining channels (6–9) are broad channels intended to characterize the surface thermal emission over a wide range of temperatures with separate filters covering ~13–23, ~25–41, ~50–100, and ~100–400  $\mu\text{m}$  (full width half max).

The ground-projected surface footprint of Diviner is dependent on spacecraft altitude which varies between ~40 and 170 km in its current elliptical orbit configuration, but is ~170 m cross-track and ~500 m in-track, accounting for spacecraft motion which results in elongation in the in-track direction, at the nominal altitude of ~50 km during the mapping mission phase (Williams et al., 2016). Each channel consists of an array of 21 detectors that are nominally nadir-pointing collecting data in a pushbroom configuration with an integration period of 0.128 s. The characteristics of the Diviner instrument are described in further detail in Paige et al. (2010a).

### 2.2. Mapping history

LRO launched on 18 June 2009 and the spacecraft commissioning phase was initiated on 27 June 2009. Diviner began acquiring data eight days later on 5 July 2009 (Fig. 2). The initial commissioning orbits were quasi-frozen ~30  $\times$  200 km polar orbits with periaxes near the lunar south pole. On 15 September 2009, LRO transitioned into a near-circular, 2 h period mapping orbit with an average altitude ~50 km (referenced to a 1737.4 km sphere) to start the Nominal Mission (Mazarico et al., 2011a). After the initial 1 year nominal mission, LRO began its two year Science Mission, during which it transitioned back into an elliptical quasi-frozen orbit on 11 December 2011. LRO is currently conducting its second extended science mission.

The time evolution of the LRO orbit geometry during the mission phases is shown in Fig. 2, encompassing the period of time that data used in the maps was acquired. The LRO orbit plane is inclined approximately 90° from the equator and is nearly fixed in inertial space. The Moon rotates 360° relative to the LRO orbit plane every 27.3 day sidereal rotation period, during which the sub-spacecraft longitude migrates 360° of longitude. This defines the length of one Diviner mapping cycle in the level 2 Global Data Records (GDR), which have been archived at the NASA Planetary Geosciences Node (LRO-L-DLRE-5-GDR-V1.0) (Paige et al., 2011). LRO obtains "daytime" coverage (defined here to be 6 am to 6 pm local solar time) during half of each orbit, and "nighttime" coverage (6 pm to 6 am local time) during the other half. As the Earth/Moon system orbits the sun, the local time of the LRO orbit shifts ~1.8 h earlier during each mapping cycle, providing full local time coverage over the course of half of an Earth Year. The

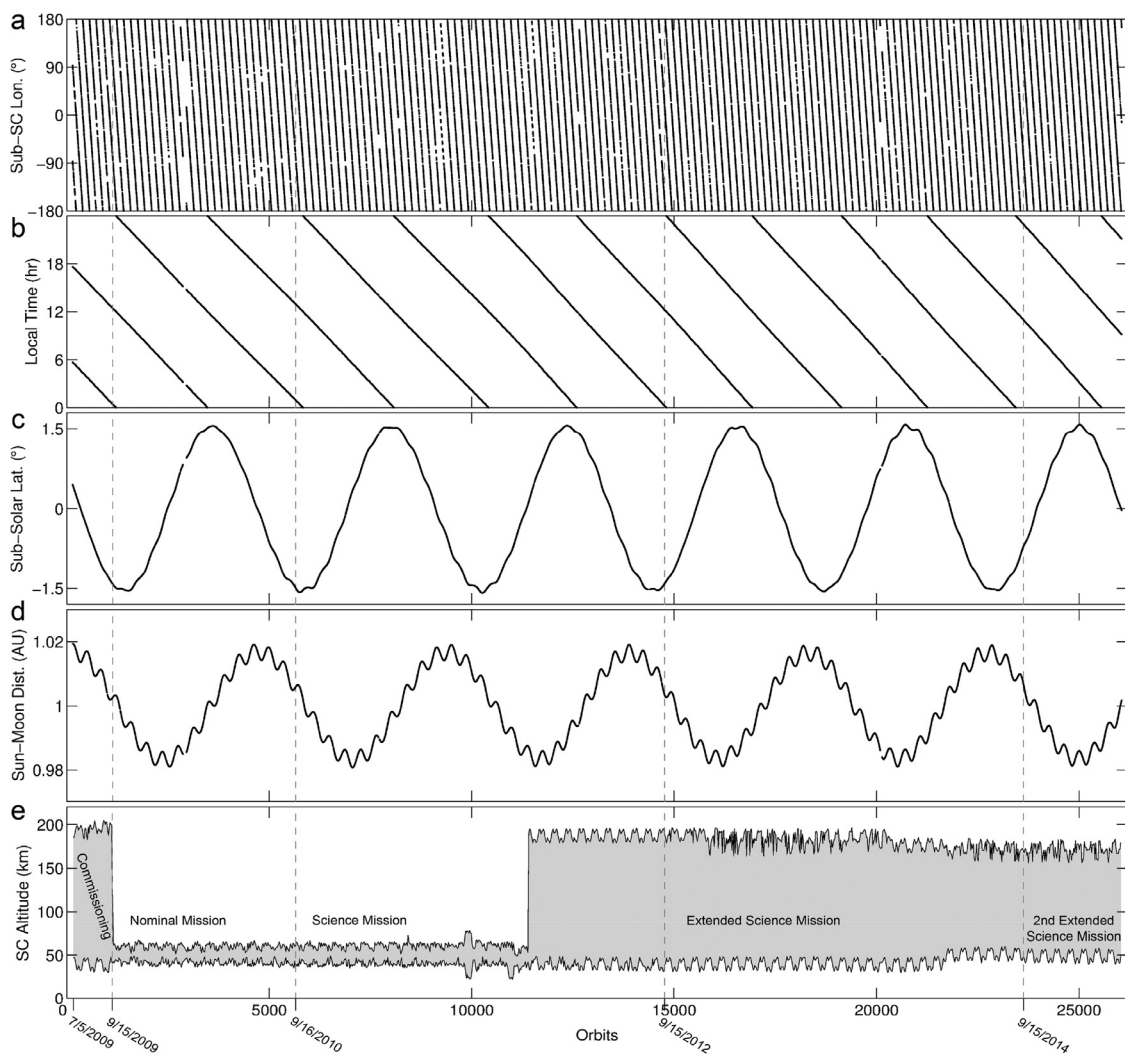


**Fig. 2.** Variations in orbital and celestial parameters within the data set used in rendering the Diviner maps. (a) The longitude and (b) local solar time beneath the space-craft's two ground tracks (i.e. the ascending and descending nodes of the orbit) at the equator. (c) The sub-solar latitude responsible for seasonal variations in insolation. (d) The distance between the centers of the Sun and Moon. (e) The spacecraft altitude relative to a spherical Moon with radius of 1737.4 km with the mission phases labeled. Vertical dashed lines denote the transitions between mission phases. The nominal mapping orbits ( $\sim 50$  km average altitude) are the near-circular orbits that start with the Nominal Mission phase and extends into the Science Mission phase, after which LRO transitioned into an elliptical orbit.

lunar spin axis is inclined by  $1.54^\circ$  relative to the ecliptic, which results in seasonal variations in insolation over the course of the 346.62 day Draconic Year (Paige et al., 2010b).

Diviner has operated nearly continuously in pushbroom nadir mapping mode to acquire a consistent global dataset with maximum coverage. Diviner's nadir mapping is routinely interrupted for space/blackbody calibrations and space/solar target calibrations, and intermittently by special off-nadir observations and campaigns as well as calibration sequences for other LRO instruments and planned and unplanned spacecraft operations activities.

### 3. Global maps

We have compiled all nadir observations (defined here to be emission angles  $< 10^\circ$  relative to a sphere) from July 5, 2009 to April 1, 2015 (over 25,000 orbits) into bins of  $0.5^\circ$  latitude and longitude and  $0.25$  h of local time. This was found to be an optimal local time resolution that adequately resolves the diurnal temperatures while providing sufficient spatial coverage at  $0.5^\circ$  resolution. Several quality constraints present in the Diviner Reduced Data Records (RDR's) available at the Planetary Data System (PDS) repository were used as well (quality flag for calibration –

0; quality flag for miscellaneous – 0; noise quality flag – 0 to 1) (Sullivan et al., 2013).

Diviner's solar channels measure the reflectance of the surface relative to the reflectance of a normally illuminated Lambertian surface (Greenhagen, 2009). An opposition surge is observed at low phase angles and at high incidence angles scattering results from topography. To minimize these effects, we generate a global visual brightness map from Diviner's channel 1 (Fig. 3) restricted to local time hours 9–10 (i.e. incidence angles  $30^\circ$ – $45^\circ$  at the equator).

For the seven Diviner infrared spectral channels, the radiance is binned into  $0.25$  h of local time from which brightness temperatures are derived. The bolometric brightness temperature,  $T_{bol}$ , is then determined from the brightness temperatures of the individual Diviner spectral channels for each  $0.5^\circ$  bin and  $0.25$  h local time, providing a diurnal temperature curve for each  $0.5^\circ$  of the lunar surface.  $T_{bol}$  is a measure of the spectrally integrated flux of infrared radiation emerging from the surface (Paige et al., 2010b). For the purposes of quantifying the overall heat balance of the surface and comparing with available models, the bolometric brightness temperature is the most fundamental and interpretable measurable quantity. With this data set, we generate global maps

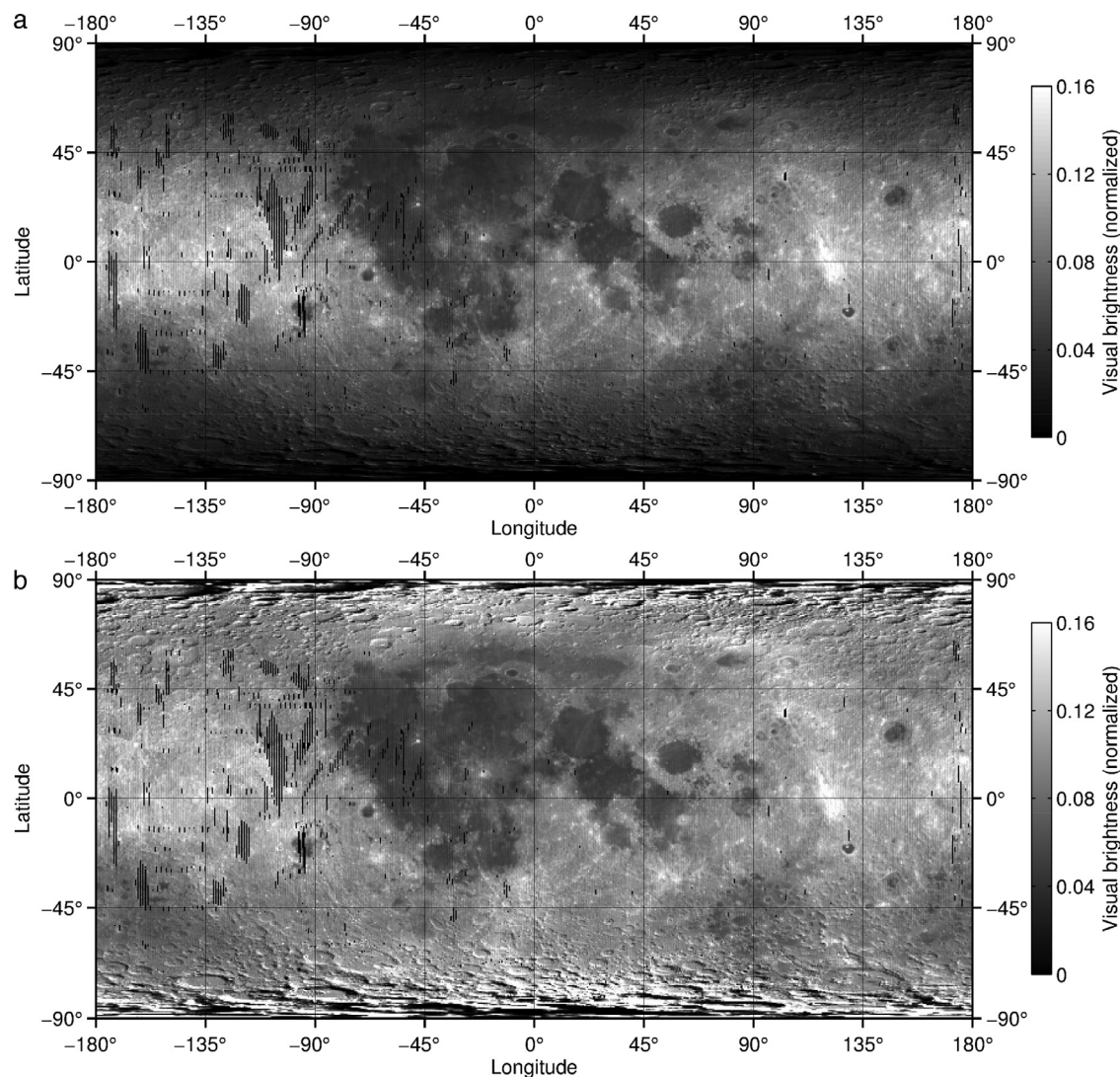


**Fig. 3.** (a) Diviner channel 1 visual brightness for local time 9–10 and (b) with a photometric normalization applied by dividing each pixel by the cosine of the latitude.

of mean hourly bolometric surface temperatures (Fig. 4) and instantaneous bolometric surface temperatures for any arbitrary subsolar longitude (Fig. 5).

To render the instantaneous global temperatures for a subsolar longitude,  $\phi_{ss}$ , the local time is determined for each 0.5° bin and the temperatures are interpolated from each 0.25 h binned local time diurnal curve. Some artifacts are observed resulting from gaps or undersampling in the local time coverage. This is particularly apparent near the dawn and dusk terminators where temperatures change abruptly resulting in sharp inflections in the diurnal curve. Unpopulated local time bins near this inflection in surface temperatures results in poorer approximations of interpolated temperatures. Further, the ground track locations from individual orbits within a bin area can vary resulting in differences in measured radiances unrelated to changing local time. The width of a ground track swath at the nominal mapping altitude of ~50 km is ~3.4 km, ~0.1° of longitude at the equator, which represents only 20% of the surface area within a bin (Williams et al., 2016). The local time resolution of 0.25°h was chosen to optimize resolution of the diurnal temperatures while minimizing empty or single orbit local time bins. Artifacts such as these result in vertical striping aligned with the near-polar LRO orbit at equatorial and mid-latitudes. Though interpolation might be improved using modeled diurnal curves fit to the data, we have not included any modeling

in the gridding procedure to avoid any model dependence on the results. The continued acquisition of data will improve the spatial and local time resolution of the Diviner data set globally and enhance future Diviner data products and science return.

#### 4. Global temperatures

##### 4.1. Bolometric temperatures and incidence angle

The highly insulating nature of the surface, the lack of an appreciable atmosphere to buffer surface temperatures, and slow rotation of the Moon allow daytime temperatures to nearly equilibrate with the solar flux. Therefore daytime temperatures are influenced by topographic effects and albedo with maximum noontime temperatures at the equator in the range ~387–397 K (Fig. 6). Temperatures were not corrected for variations in the Moon-sun distance prior to binning, therefore maximum temperatures are for all orbital configurations. The zonal mean noon temperatures (Fig. 7) decrease with latitude,  $\theta$ , consistent with the  $\cos^{1/4}(\theta)$  shape observed for daytime temperatures by the Clementine long wave infrared (LWIR) camera (Lawson et al., 2000). The lunar regolith is highly insulating due to its low density and thermal conductivity (Linsky, 1966; Cremers and Birkebak, 1971; Keihm and Langseth; 1973) and therefore heat flow into

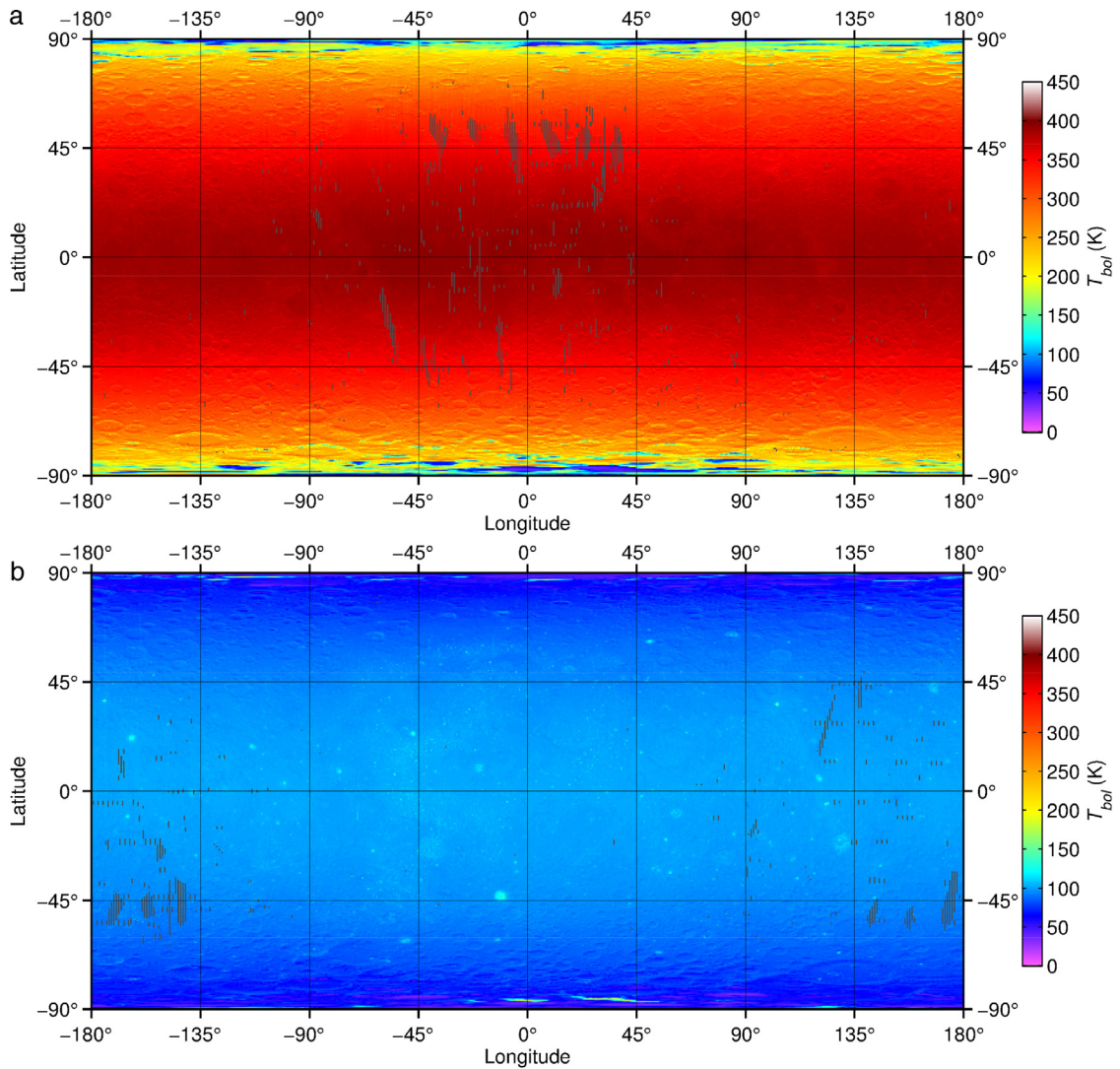


**Fig. 4.** Mean global bolometric temperatures for one hour of local time centered on (a) noon and (b) midnight.

the subsurface during the day is small compared to the incident solar flux (Vasavada et al., 1999, 2012). Daytime temperatures can therefore be approximated from the balance of incoming solar flux and outgoing thermal emission:

$$T(\theta) = [S(1 - A) \cos(\theta)/\varepsilon\sigma]^{1/4} \quad (1)$$

where  $S$  is the solar constant,  $A$  is albedo,  $\varepsilon$  is emissivity, and  $\sigma$  the Stefan-Boltzmann constant. Similar to Vasavada et al. (2012), we find that temperatures require the albedo to increase with latitude (Fig. 7). Using the albedo from Vasavada et al. (2012):

$$A(\theta) = A_0 + a(\theta/45)^3 + b(\theta/90)^8$$

where  $a = 0.045$  and  $b = 0.14$  and assuming  $A_0 = 0.08$ ,  $S = 1370$ , and  $\varepsilon = 0.95$  provides similar temperatures to the observed mean zonal temperatures and is similar to the analytic function derived by Hurley et al. (2015). The standard deviation of the mean  $T_{bol}$  also increases with latitude. While  $T_{bol}$  variations near the subsolar point will be largely due to variations in albedo and emissivity (Fig. 6), at higher incidence angles, the influence of topography and surface roughness on temperatures will dominate resulting in increasing variations in temperatures for a given local time.

Temperatures are observed to decrease with latitude at all local times (Fig. 8) with the largest amplitude in diurnal temperatures occurring at the equator (Fig. 9). Temperatures between noon and

midnight at the equator vary  $\sim 290$  K while at  $85^\circ$  latitude, the temperature variation is reduced to  $\sim 120$  K. Changes in temperatures occur particularly rapidly in the early morning and late afternoon local times. Temperatures increase  $> 150$  K from hour 6 to 7 at the equator. The standard deviation of the mean temperatures is also relatively large during these hours as slopes and shadows will have the largest influence on temperatures (Figs. 8b and 9b).

Nighttime temperatures by comparison are much more uniform (Fig. 8c-d). Nighttime temperatures are characterized by cold temperatures with the sensible heat stored in the subsurface during the day being the only heat source to balance the loss of thermal radiation to space during the long lunar night. As a result, surface temperatures are sensitive to the thermophysical properties of the near-surface regolith. Rocky, coherent surfaces and blocks with higher thermal inertia provide larger reservoirs of heat and remain warmer than the pulverized, fine-grained regolith (Bandfield et al., 2011; Williams et al., 2016). Temperatures decrease throughout the night with the mean temperatures at the equator decreasing from  $\sim 117$  K to  $\sim 95$  K between the hours 19 and 5 (Fig. 8c). The rate of cooling declines as surface temperatures decrease and heat is conducted to the surface from increasing depth through the night. From hours 19 to 20, equatorial temperatures cool 5.4 K compared with 1.0 K between the morning hours 4 and 5 prior to sunrise. Modeling by Vasavada et al. (2012) has shown that the

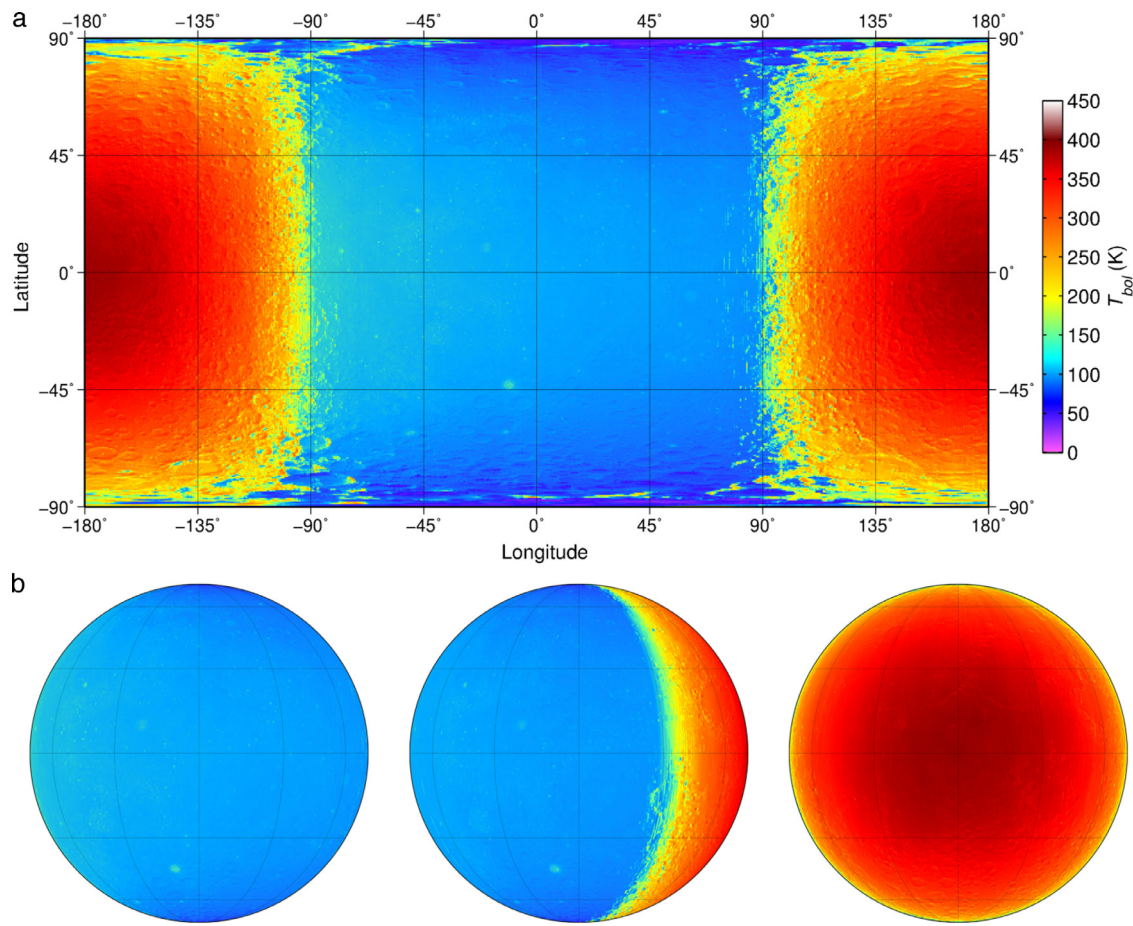


**Fig. 5.** Global instantaneous temperatures of the Moon in (a) cylindrical equidistant projection ( $\phi_{ss} = 180^\circ$ ) and (b) orthographic projection ( $\phi_{ss} = 180^\circ$ ,  $120^\circ$ , and  $0^\circ$ ).

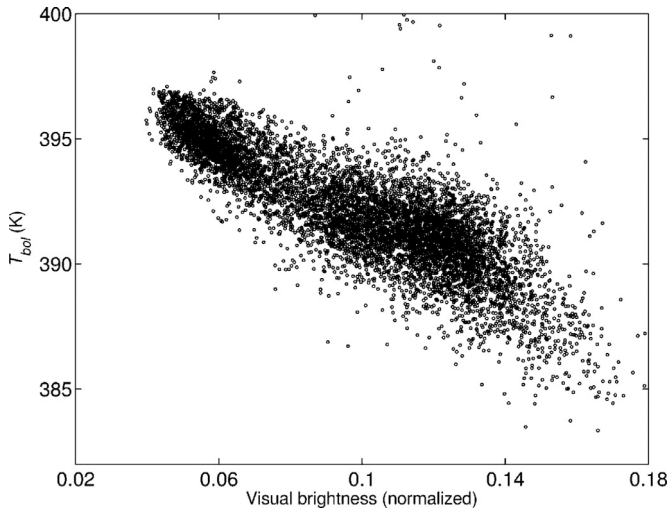


**Fig. 6.** Maximum bolometric temperatures at the equator (within  $\pm 5^\circ$  latitude) and the corresponding relative surface reflectance from Diviner channel 1 (Fig. 3b).

equatorial nighttime temperatures are consistent with an exponential increase in density and thermal conductivity with depth.

An asymmetry is observed between morning and afternoon daytime temperatures. This is observed as an offset in temperatures between morning and afternoon temperatures with equivalent solar incidence angles (Fig. 6a). This asymmetry increases with increasing incidence angle. For example equatorial

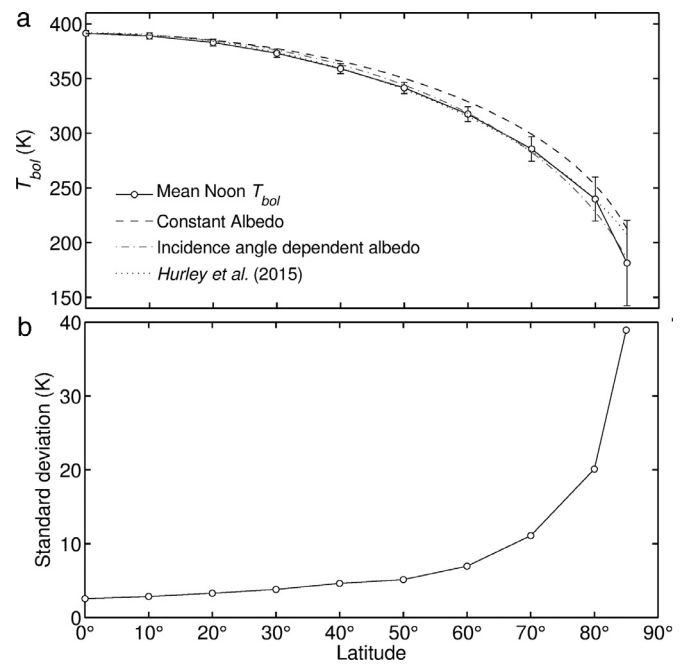


**Fig. 7.** (a) Zonal mean noontime bolometric temperatures. Error bars are standard deviations plotted in (b). Curves are temperatures assuming radiative balance for a constant albedo (dashed) and incidence angle dependent albedo (dash-dot) of Vasavada et al. (2012), and the analytic function (dot) from Hurley et al. (2015).

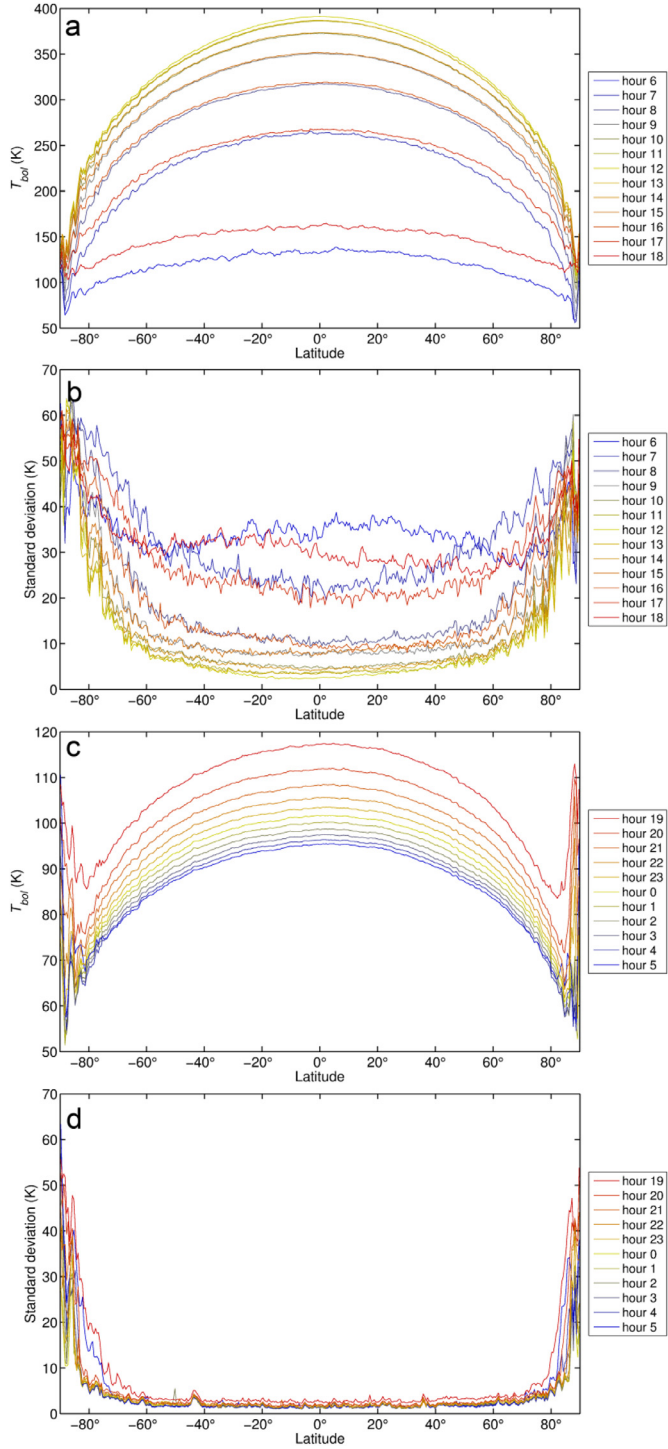


**Fig. 8.** (a) Zonal mean hourly daytime bolometric temperatures and (b) standard deviation. (c) Zonal mean hourly nighttime bolometric temperatures and (b) standard deviation. Higher nighttime temperatures and standard deviations at latitudes above  $\pm 80^\circ$  in (c-d) result from the occurrence of low-angle illumination of surfaces, especially during polar summers. Nighttime is defined here by local time, not sun elevation.

temperatures at hour 6 (dawn terminator) is  $\sim 133$  K and hour 18 (dusk terminator) is  $\sim 163$  K, a difference of  $\sim 30$  K. Temperatures at hours 7 and 17 are  $\sim 263$  K and  $\sim 267$  K respectively, a difference of  $\sim 4$  K and temperatures at hours 8 and 16 are  $\sim 317$  K and  $\sim 318$  K. The offset also appears to be larger at higher latitudes. [Bandfield et al. \(2015\)](#) found that non-radiative-equilibrium conditions are

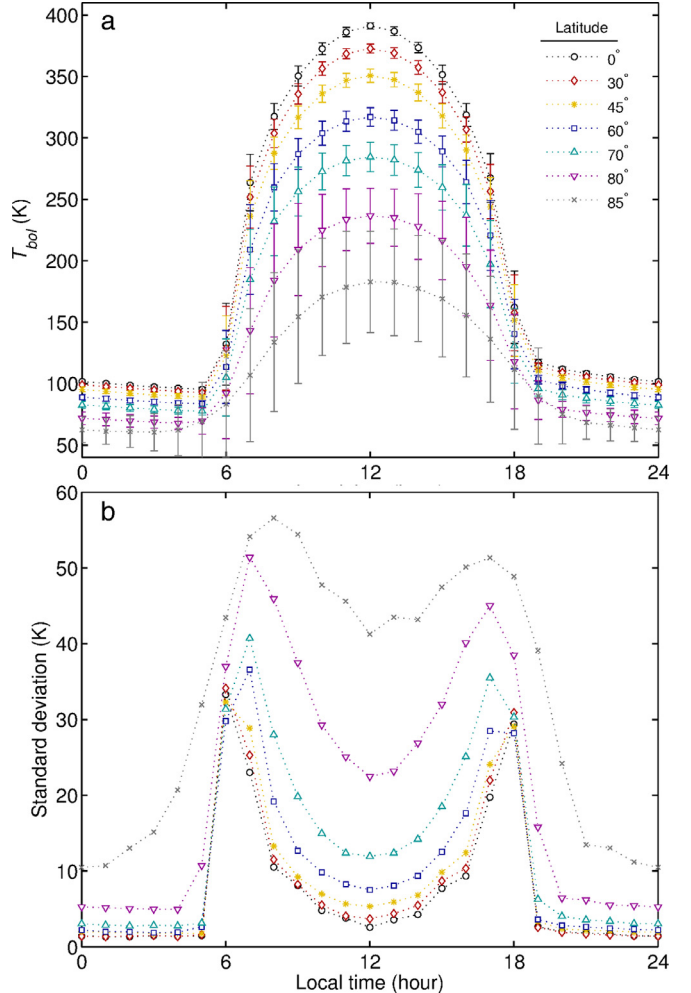


**Fig. 9.** (a) Zonal mean bolometric temperatures and (b) standard deviation versus local time for latitude bands  $0^\circ$ ,  $30^\circ$ ,  $45^\circ$ ,  $60^\circ$ ,  $70^\circ$ ,  $80^\circ$ , and  $85^\circ$ .

prevalent at local times approaching sunrise and sunset and high latitudes where illumination conditions are changing rapidly and sunlit and shaded surfaces can be cooler or warmer respectively than predicted by models assuming equilibrium conditions.

The effects of thermal inertia can also be observed when comparing morning and afternoon temperatures with incidence angle globally (Fig. 10). We generate instantaneous surface temperatures as described in Section 3 (Fig. 5) for every  $15^\circ$  of subsolar longitude. The 24 global temperature maps represent 24 h of the lunation cycle. These maps are then shifted in longitude so the subsolar longitudes co-align providing an average of the temperatures in relation to the subsolar point (Fig. 10a). The daytime temperatures are split into *am* (hours 6–12) and *pm* (hours 12–18) local times and binned into  $5^\circ$  increments of incidence angle (Fig. 10b). Mean temperatures are increasingly higher in the *pm* hours than the *am* hour at increasing incidence angle with a difference of 10 K at  $85^\circ$ .

#### 4.2. Anisothermality

##### 4.2.1. Daytime

Brightness temperatures in Diviner's individual infrared channels may vary depending on the distribution of sub-footprint-scale temperatures, spectral emissivities, and photometric properties. In general, Diviner's surface footprint contains small scale slopes, shadows, or rocks, resulting in a mixture of temperatures within the field-of-view. Due to the non-linear nature of Planck radiance

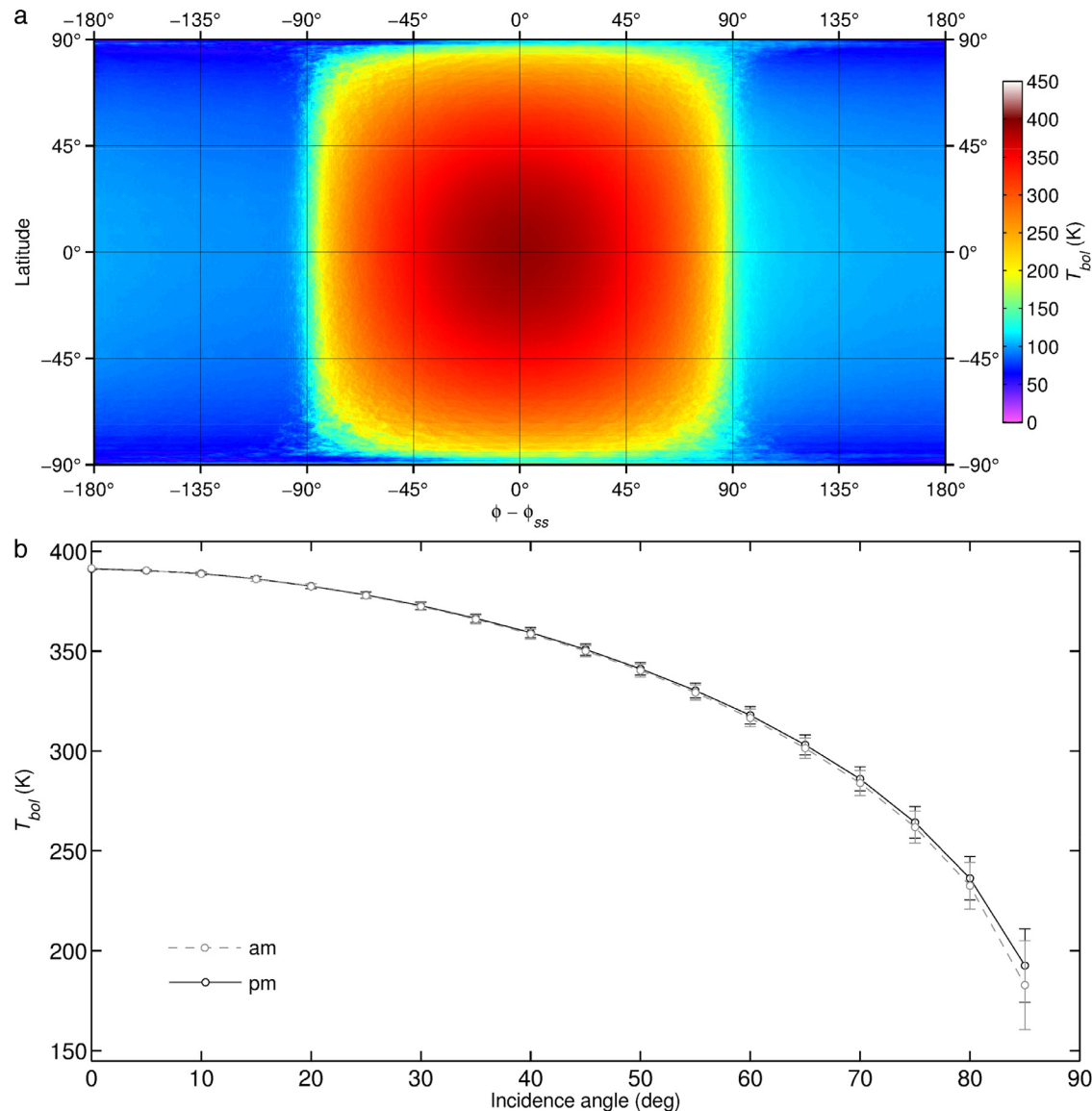


**Fig. 10.** (a) Average of 24  $T_{bol}$  maps generated with  $15^\circ$  increments of subsolar longitude normalized to the subsolar point ( $0^\circ$ ,  $0^\circ$ ). (b) Mean daytime  $T_{bol}$  from (a) for morning hours 6–12 (grey) and afternoon hours 12–18 (black) as a function of incidence angle binned at  $5^\circ$  intervals. Error bars are the standard deviation.

with respect to wavelength, the warmer temperatures have an increased proportional influence on brightness temperatures in the shorter wavelength channels. Therefore the brightness temperatures cannot be interpreted in terms of a unique surface temperature. The bolometric temperature, by integrating the full spectrum, is more directly related to the heat balance of the surface. However, the anisothermality in the individual Diviner channels provides information about surface roughness (Bandfield et al., 2015) and heterogeneities in thermophysical properties (Bandfield et al., 2011).

At high incidence angles, sunlit slopes and shadows result in a variety of temperatures depending on slope orientations with respect to the sun. Large lateral temperature gradients are possible due to the highly insulating nature of the top few cm of the regolith with surfaces separated by distances a few mm able to remain thermally isolated in the lunar environment (Bandfield et al., 2015). The mixture of sunlit and shaded slopes in the early morning and late afternoon hours results in elevated anisothermality observable by differencing the brightness temperatures of individual Diviner channels. Fig. 11 shows a difference map of Diviner

channels 4 (8.10–8.40  $\mu\text{m}$ ) and 7 (25–41  $\mu\text{m}$ ) daytime temperatures with the subsolar longitude and latitude at  $0^\circ$ . The channel 4 passband is near the observed mean CF emission peak (8.15 for highlands, 8.30 for mare; Greenhagen et al., 2010) and observed temperatures are consistently  $\sim 5$ –7 K warmer than channel 7 for incidence angles  $< 30^\circ$  (Fig. 12). The  $T_4$ – $T_7$  anisothermality increase with incidence angle results from surface roughness where shadowing and slope effects lead to mixtures of temperatures within the field-of-view and are maximized at incidence of  $90^\circ$  representing the poles and the terminators where illumination is at grazing angles. Channel 4 loses sensitivity below  $\sim 190$  K resulting in some anomalous low, or negative anisothermality values near the poles and the nighttime hours.

Bandfield et al. (2015) showed that surface roughness had little effect on anisothermality for incidence angles less than  $\sim 30^\circ$  and the observed difference in brightness temperatures at these angles is predominantly due to differences in emissivity for the two channel's passband wavelengths. These emissivity differences are highlighted by subtracting the zonal mean anisothermality from maps with local times constrained to  $\pm 2$  h of local time around

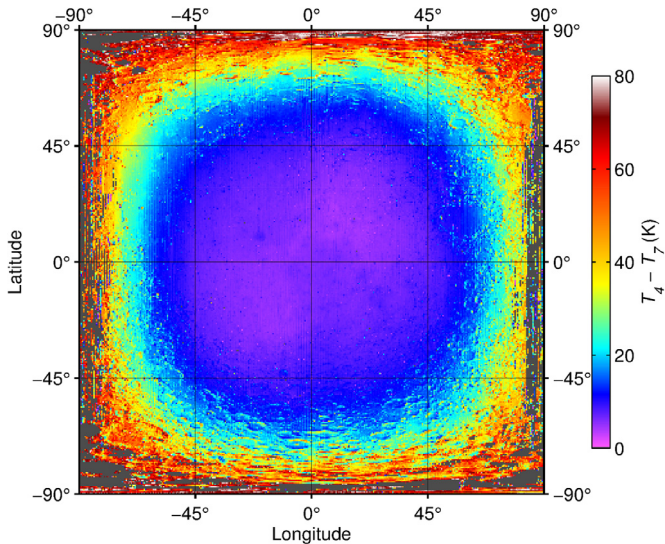


**Fig. 11.** Daytime brightness temperature difference between Diviner channels 4 and 7 for subsolar longitude and latitude 0°. Grey areas are where channel 4 loses sensitivity below  $\sim 190$  K.

noon (Fig. 13). The observed variations in emissivity of  $T_3-T_7$  and  $T_4-T_7$  are shown in Fig. 13. Channel 4 is typically near the peak in the Christiansen feature and less susceptible to emissivity variations than channel 3. This is apparent in Fig. 13 where the  $T_3-T_7$  map displays larger emissivity variations than  $T_4-T_7$ . This demonstrates that emissivity varies to a greater extent near 8  $\mu\text{m}$  than at the channel 7 passband (26–41  $\mu\text{m}$ ) and the variation in anisothermality observed in the maps result from shifts in the CF wavelength position (Greenhagen et al., 2010). The maria and regions containing extensive pyroclastic deposits such as Aristarchus Plateau, Sulpicius Gallus, Mare Vaporium, Rimae Bode, exhibit typically smaller emissivity differences while highly reflective surfaces, such as the immature materials excavated by young impacts, including rays in some cases (e.g. Tycho and Jackson craters), show larger emissivity differences. These variations correspond to the variation in CF mapped by Greenhagen et al. (2010).

#### 4.2.2. Nighttime

Anisothermality in nighttime temperatures is indicative of materials with differing thermophysical properties within Diviner's field-of-view. Bandfield et al. (2011) modeled anisothermality in Diviner channels 6–8 to derive rock abundances and regolith fines temperature. We have created a global nighttime average anisothermality map using the mean brightness temperatures for the local time range 20–4 from Diviner channels 6 (13–23  $\mu\text{m}$ ) and 8 (50–100  $\mu\text{m}$ ) which provide the largest nighttime anisothermal contrast (Fig. 14). The signal-to-noise ratio for the shorter wavelength channels is not adequate for the relatively cold lunar nighttime temperatures and channel 9 has relatively large drifts in brightness temperature following calibration sequences that result in striping artifacts in channel difference maps.

The nighttime  $T_6-T_8$  map reveals broad global variations in regolith thermophysical properties within the top  $\sim 30$  cm, the approximate penetration depth of the diurnal thermal wave (Vasavada et al., 2012). High  $T_6-T_8$  values represent locations where temperature contrasts occur within Diviner's field-of-view during the lunar night, for example areas with various fractions of rocks and regolith fines with highly contrasting thermal inertias (Bandfield et al., 2011). The largest values correspond to young Copernican-age impact craters that have excavated large blocks such as Tycho crater ( $43.4^\circ\text{S}, -11.3^\circ\text{E}$ ). The age of Tycho is  $\sim 100$  Ma

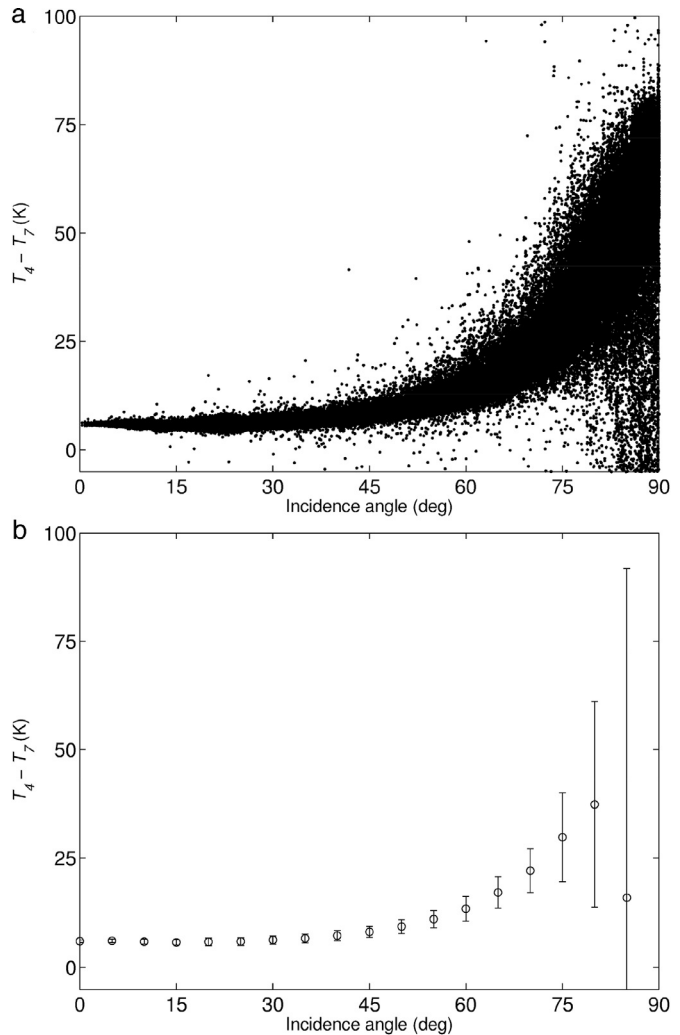


**Fig. 12.** (a) Scatter plot and (b) binned values of Diviner channel 4–7 brightness temperatures versus incidence angle for subsolar longitude and latitude 0°. Error bars are standard deviation.

(Stöffler and Ryder, 2001) and likely the youngest crater of its size ( $D=86$  km). The pattern of anisothermality also reflects the distribution of maria and regolith that has been disturbed or modified by impact events such as the emplacement of rays or impact melts.

Rocks and coherent blocks on the surface of the Moon will be mechanically broken down into fine-grained regolith by micrometeorite bombardment, the dominant surface geologic process operating on the Moon. Ghent et al. (2014) found a strong inverse correlation between the 95th percentile value of Diviner derived rock abundance for the ejecta of Copernican-age craters and their published model crater-retention ages. The implied rate of breakdown of large ejecta blocks is qualitatively consistent with the estimated survival times of meter-sized boulders from LRO Camera (LROC) images. Basilevsky et al. (2013) find that for boulders  $\geq 2$  m in diameter, 50% of the original rock population will be destroyed after  $\sim 40$ –80 Ma. These implied survival times are about a factor of 5 shorter than pre-LRO estimates (Horz et al., 1975). Vasavada et al. (2012) noted a general thermophysical homogeneity implied by Diviner observations near the equator due to the ubiquitous bombardment of the lunar surface that has pulverized material into fine grains. However, as the  $T_6-T_8$  map shows, differences in the bulk properties of the surface and near-surface do persist.

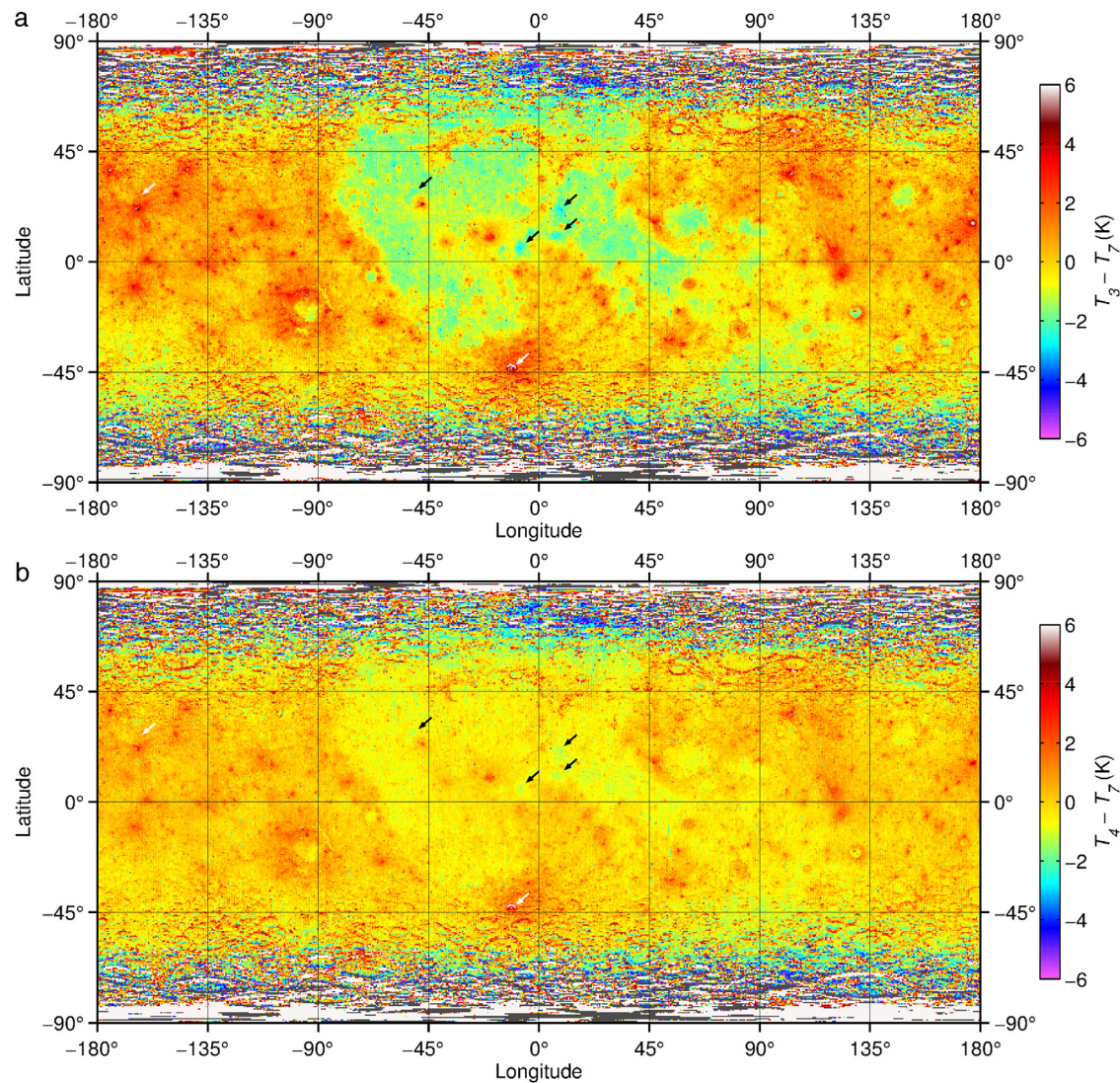


**Fig. 13.** Zonal mean (a)  $T_3 - T_7$  and (b)  $T_4 - T_7$  averaged over a 4 h local time window centered on noon (hours 10–14) corresponding to incidence angles  $\leq 30^\circ$  at the equator. Black arrows are large pyroclastic deposits with below average anisothermality and white arrows are examples of immature, high-reflectance surfaces with above average anisothermality associated with the Copernican-age craters Jackson and Tycho.

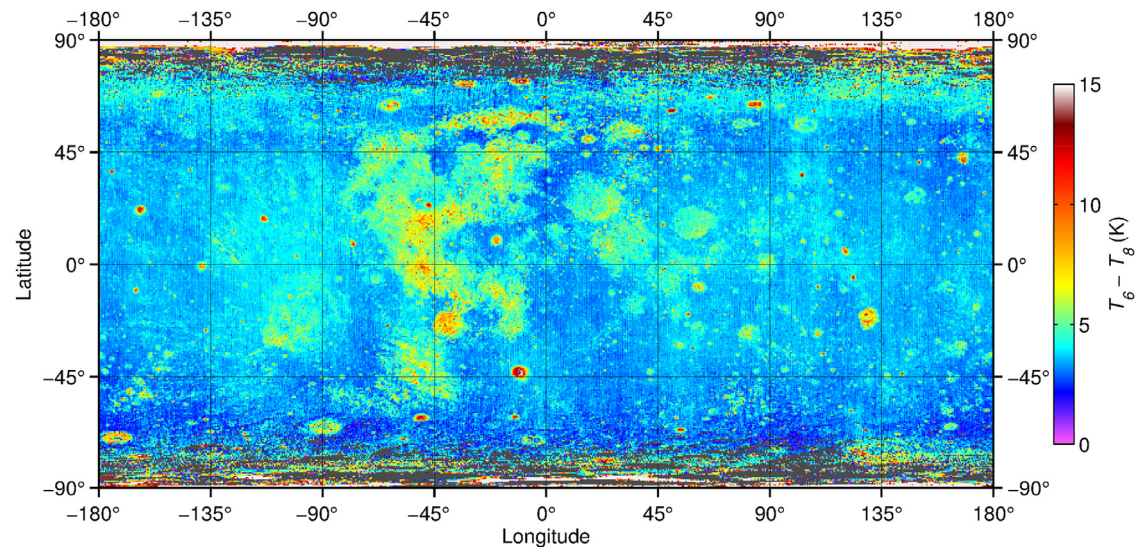


**Fig. 14.** Mean nighttime (local time hours 20–4) brightness temperature difference between Diviner channels 6 and 8. Grey areas near the poles are where channel 6 loses sensitivity below  $\sim 95$  K.

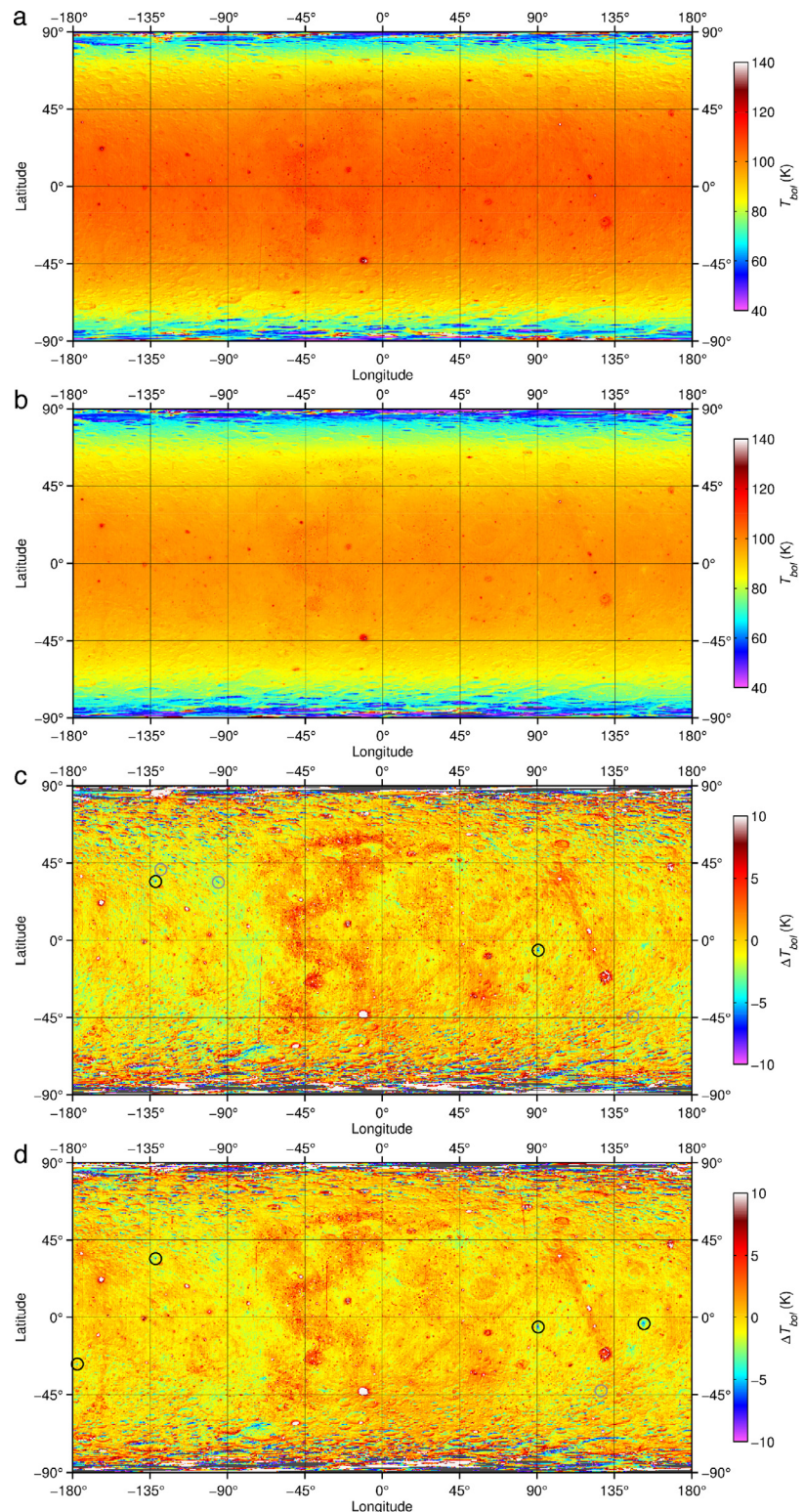


**Fig. 15.** (a) Early nighttime temperatures (hours 20–0) and (b) late nighttime temperatures (hours 0–4). (c) Early nighttime temperature anomalies and (d) late nighttime temperature anomalies. The circles are the locations of the five coldest temperature anomalies within  $\pm 45^\circ$  latitude. Black circles are cold spots and grey circles are poleward facing slopes.

#### 4.3. Nighttime temperature anomalies

Anomalous nighttime temperatures are highlighted by subtracting the zonal mean temperature from the global temperatures,  $\Delta T_{bol} = T_{bol} - T_{zonal\ mean}$ . Surface temperatures are highly sensitive to properties such as density and particle size distribution. Slight

modifications to the grain packing or concentration of rocks can result in a temperature contrast relative to typical lunar regolith that can be readily detected in Diviner observations (e.g., Bandfield et al., 2011; Hayne et al., 2013; Vasavada et al., 2012; Yu and Fa, 2016). Similar to the nighttime  $T_6-T_8$  map, these  $\Delta T_{bol}$  maps reveal areas of atypical thermophysical properties (Fig. 15). Note that

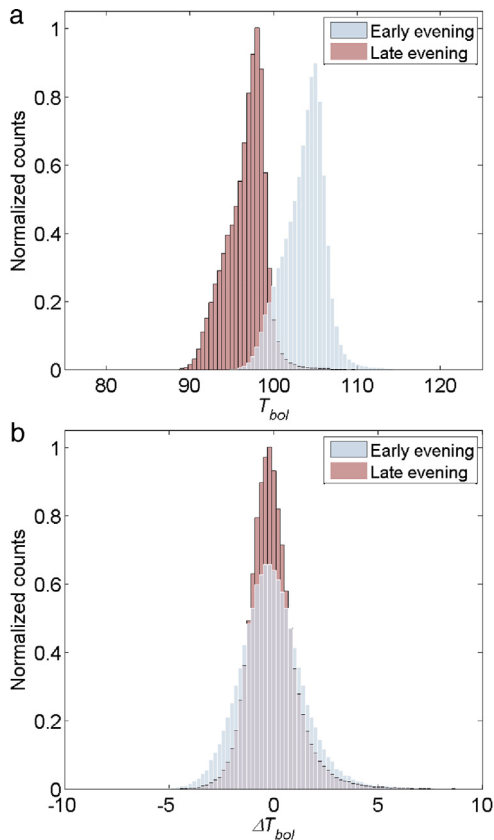


**Fig. 16.** Histograms of (a) early (hours 20–0) and late (hours 0–4) nighttime temperatures and (b) early and late nighttime temperature anomalies within  $\pm 45^\circ$  latitude.

the  $T_6-T_8$  values do not necessarily correlate with the anomalous nighttime temperatures. A surface of uniform temperature within Diviner's field-of-view will not result in anisothermality regardless of whether that surface is anomalously warm or cool for a given latitude and local time as anisothermality results from a mixture of temperatures within the instruments field of view.

We have split the temperatures into early nighttime (hours 20–0) and late nighttime (hours 0–4) to create mean global temperature maps of the early and late nighttime and corresponding early and late nighttime temperature anomaly maps (Fig. 15). Histograms of the temperatures within  $\pm 45^\circ$  latitude (Fig. 16) show the relative cooling between the early and late hours with the peaks of the histograms shifting from 105 K to 98 K. The histograms of the temperature anomalies show a reduction in temperature differences in the late nighttime implying a homogenization of temperatures over time. This could result from a reduction in thermal contrast between sloped surfaces or high and low thermal inertia materials, or a reduction in contrasting thermophysical properties at deeper levels of the regolith as heat is conducted from greater depths later in the night.

The five coldest temperature anomalies in the early nighttime and the late nighttime maps within  $\pm 45^\circ$  latitude are marked with circles in Fig. 15c and d respectively. The black circles are locations that contain cold spots: thermal features characterized by small, fresh craters surrounded by extensive distal, highly insulating surfaces (Bandfield et al., 2014). Two of these cold spots appear in both the early and late nighttime anomaly maps at map pixels centered on 5.75°S, 90.75°E and 34.25°N, −131.75°E. Two additional cold spot at 3.25°S, 152.25°E and 27.25°S, −177.25°E are among the coldest temperature anomalies in the late evening map. These four cold spots persist as cold temperature anomalies

in the late nighttime with  $\Delta T_{bol}$  values of −8.4, −6.9, −6.2 and −5.6 K. The other locations identified as having large  $\Delta T_{bol}$  values are associated with poleward facing slopes near the  $45^\circ$  latitude cutoff implying slopes begin to influence temperatures to a larger extent near this latitude. All but one are identified in the early map indicating that, unlike the cold spots, their thermal contrast diminishes over time. The average temperatures of the cold spots for each hour of local time between hours 20 and 4 is plotted in Fig. 17. The cold spots maintain their approximate  $\Delta T_{bol}$  values throughout the night without converging toward the mean temperatures of the corresponding latitude explaining why cold spots become more apparent as thermal anomalies later in the night.

The hottest temperature anomalies are associated with the young rayed Copernican-age craters Giordano Bruno, Tycho, and Moore-F with average nighttime temperatures of 149.4, 141.3, and 135.4 K respectively for the warmest map pixels at each crater which represent  $\Delta T_{bol}$  values of 50.9, 45.0, and 36.3 K. These craters are associated with high rock abundances and bright rays. Unlike the cold spots, their thermal contrast diminishes over time during the night (Fig. 17b). Localized surfaces likely have even warmer nighttime temperatures. These temperature anomalies are an average of the area represented by the  $0.5^\circ$  binned data and isolated regions at smaller spatial scales that are unresolved at this resolution will be hotter. Areas such as these may be of importance for exploration and long-duration surface missions as the warmer nighttime temperatures reduce the temperature extremes experienced by hardware deployed on or near the lunar surface. Significant variations in temperature complicate the design of habitats and other structures due to thermal expansion and contraction and can lead to structural fatigue (e.g. Ruess et al., 2006; Mottaghi and Benaroya, 2015; Malla and Brown, 2015).

#### 4.4. Minimum and maximum temperatures

Daytime temperatures on the Moon are approximately in radiative equilibrium. For slowly rotating bodies with low thermal inertias like the Moon, heat diffusion models predict surface temperatures at the equator within  $\sim 1$  K of radiative equilibrium between local time hours 8 and 16 (i.e. incidence angles  $< 60^\circ$ ) (Vasavada et al., 2012; Bandfield et al., 2015). Maximum temperatures therefore occur at noon and will depend on the albedo while being sensitive to the orbital and celestial geometry. The minimum temperatures will occur just prior to local sunrise and are dependent on the thermophysical properties of the near-surface.

Maximum and minimum global surface temperature maps are shown in Fig. 18. The mean temperature at the equator is 215.5 K with an average maximum of 392.3 K and average minimum of 94.3 K (Fig. 19), representing an average change in temperature of  $\sim 300$  K. Average maximum and minimum temperatures in the polar regions (poleward of  $85^\circ$ ) are 202 K and 50 K respectively with a mean average temperature 104 K. Mean maximum temperatures in the south polar region are  $\sim 11$  K warmer than the north polar region, however the average minimum temperatures are the same at both poles. This discrepancy is likely due to differences in the distribution and configuration of the topography which is the dominant control of polar temperatures on the Moon. The south polar topography is more rugged, displaying a larger range of elevations (Smith et al., 2010). The maximum solar declination of  $1.54^\circ$  results in surfaces that are permanently shadowed down to roughly  $60^\circ$  latitude (McGovern et al., 2013; Siegler et al., 2015). Though a larger surface fraction of the south polar region is in permanent shadow compared to the north polar region, the larger topography range responsible for this results in generally more favorable illumination conditions for equator facing slopes than in the north (Mazarico et al., 2011b).

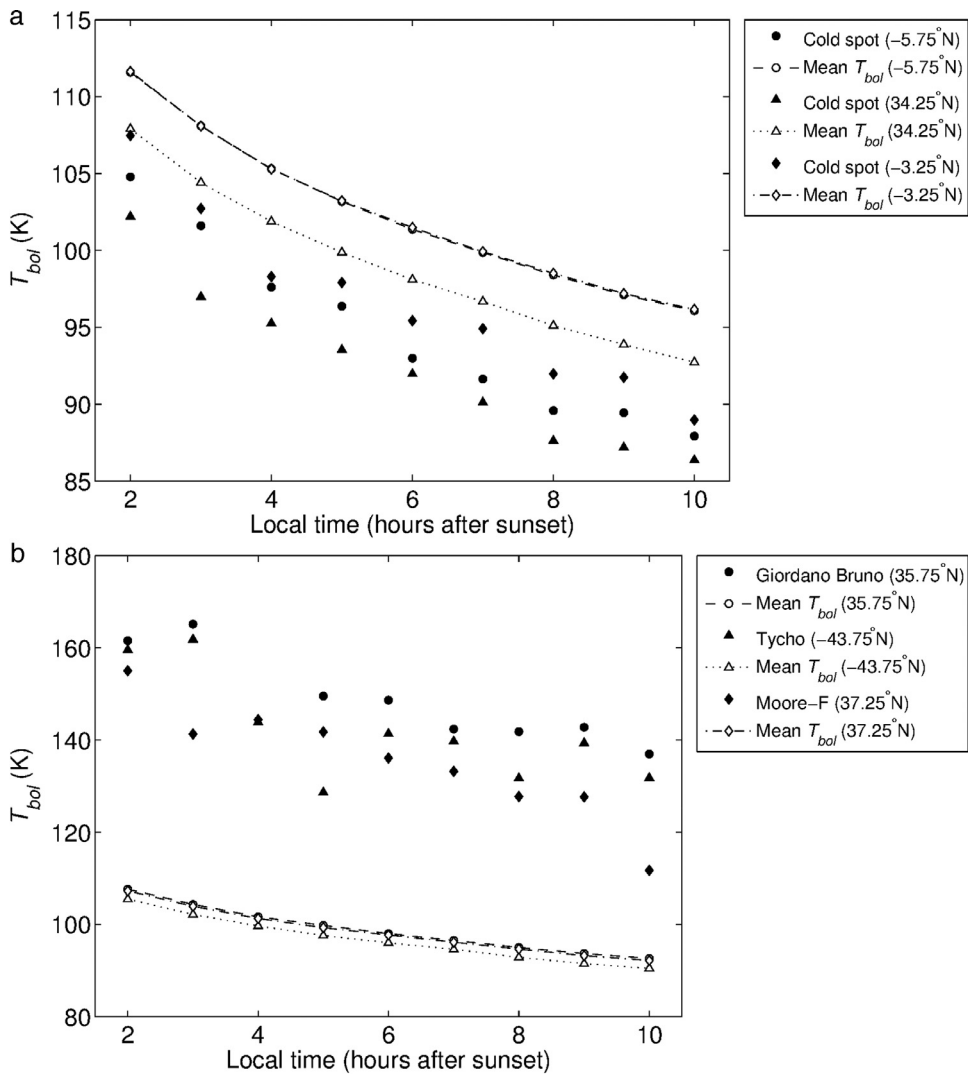


**Fig. 17.** Hourly average nighttime  $T_{bol}$  for (a) three lowest temperature anomaly cold spots and (b) three hottest temperature anomaly bright-rayed Copernican craters along with the average  $T_{bol}$  for their corresponding latitudes.

The latitude effects on the maps are removed by subtracting the zonal mean minimum and maximum temperatures (Fig. 20), as was done in Section 4.3 to highlight nighttime temperature anomalies (Fig. 15). Like the nighttime temperature anomalies, minimum temperature anomalies are related to thermophysical properties while maximum temperature anomalies are related to albedo. Darker surfaces have higher maximum temperatures relative to bright surfaces, while high thermal inertia (TI), or rocky surfaces have high minimum temperatures relative to low-TI surfaces (Fig. 21).

The ratio of the maximum and minimum temperatures,  $T_{max}/T_{min}$ , highlights relative differences between the temperatures while differencing the minimum and maximum temperatures,  $T_{max} - T_{min}$ , shows the absolute difference, or amplitude, between the two temperature extremes (Fig. 20). While these are similar in that they both convey information about variations between the maximum and minimum temperatures, they do not necessarily correspond;  $T_{max}/T_{min}$  can remain the same between two locations while  $T_{max} - T_{min}$  does not, and vice versa. For example, if  $T_{min} = 80$  K and  $T_{max} = 250$  K at location A ( $T_{max} - T_{min} = 170$  K) and  $T_{min} = 112$  K and  $T_{max} = 350$  K at location B ( $T_{max} - T_{min} = 238$  K), then  $T_{max}/T_{min} = 3.125$  at both locations. Alternately if we compare

location B to a new location C with  $T_{min} = 80$  K and  $T_{max} = 318$  K,  $T_{max} - T_{min} = 170$  K at both locations, however  $T_{max}/T_{min} = 3.975$  at location C. In other words, for a given amplitude, shifting the minimum and maximum temperatures downward increases the ratio. As a result,  $T_{max}/T_{min}$  is more sensitive to smaller amplitude differences at colder temperatures relative to  $T_{max} - T_{min}$ . The cold spots provide a good example of this as they have large positive values in the ratio anomaly map, but are not as apparent in the difference anomaly map (Fig. 20). Being correspondingly larger at lower temperatures,  $T_{max}/T_{min}$  is also less sensitive to slope effects at high latitudes as poleward and equator facing slopes at a given latitude have similar relative  $T_{max}/T_{min}$  values.

The absolute difference between the maria and highlands is apparent in the  $T_{max} - T_{min}$  anomaly map, however the relative difference between them is similar. This lack of distinction between the two terrains in the  $T_{max}/T_{min}$  map results from the diurnal modulation of temperatures occurring at higher temperatures in the maria. The region in the black box in Fig. 20, for example, is a region of fairly homogenous  $T_{max}/T_{min}$  values though they include both highland and mare units. The  $T_{max} - T_{min}$  values however differ between maria and highlands reflecting a higher temperature amplitude in the mare.

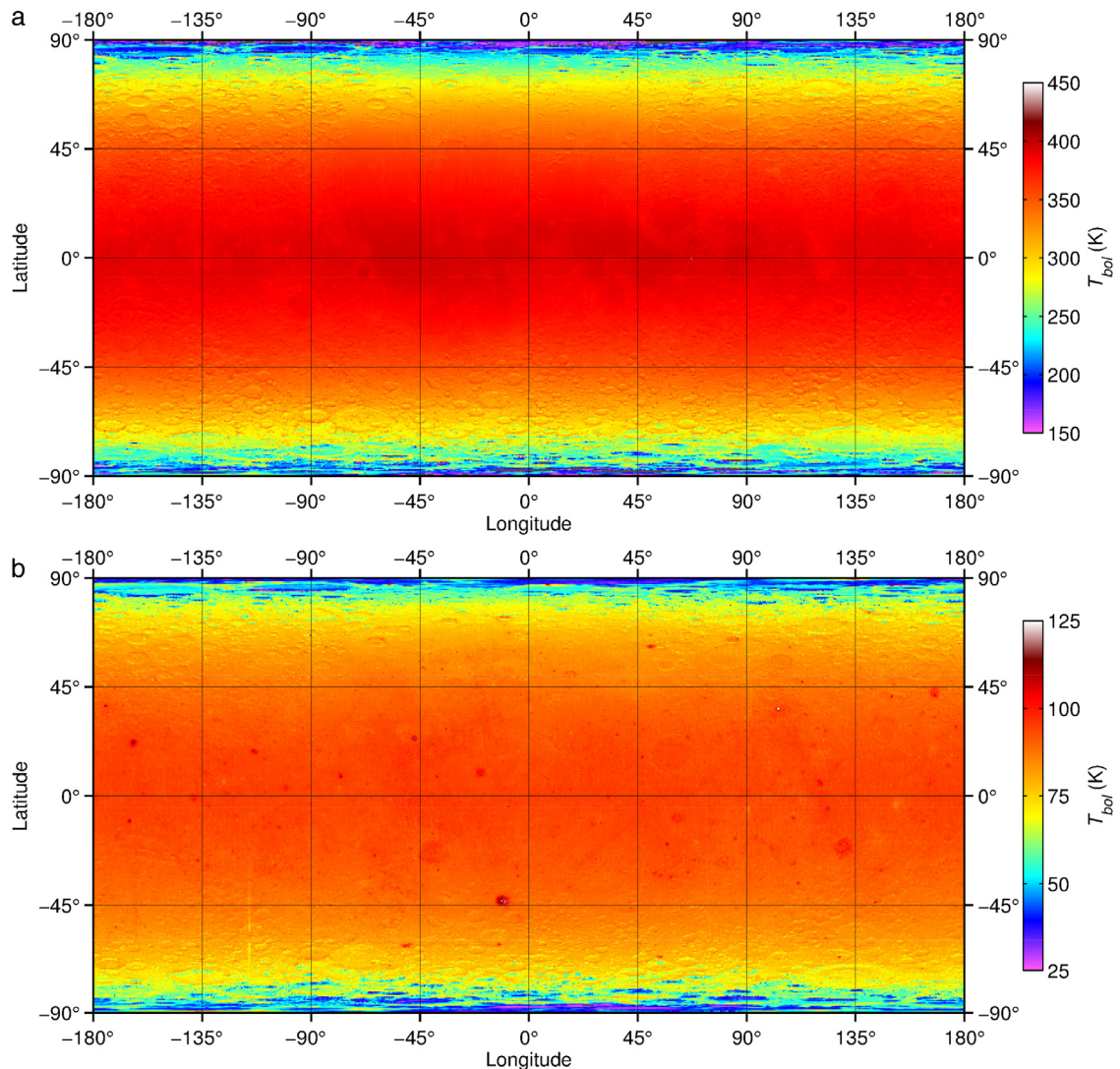


**Fig. 18.** (a) Maximum and (b) minimum global temperatures.

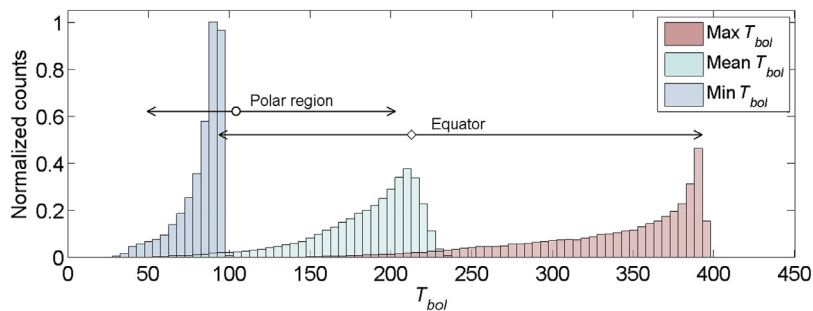


**Fig. 19.** Histograms of maximum, mean, and minimum global temperatures. The mean temperature at the equator ( $\diamond$ ) is 215.5 K with an average maximum of 392.3 K and average minimum of 94.3 K (arrows show range between average maximum and minimum  $T_{bol}$ ). The mean temperature of the polar regions poleward of  $85^\circ$  ( $\circ$ ) is 104 K with an average maximum of 202 K and average minimum of 50 K (arrows show range between average maximum and minimum  $T_{bol}$ ).

## 5. Discussion

### 5.1. Copernican-age craters

Many young, Copernican-age craters are associated with bright, high-reflectance surfaces within their interiors, blocky ejecta, and rays as fresh excavated subsurface material is generally brighter than surrounding surface materials. This modification

of the regolith by impacts is apparent in the thermal data as the addition of blocky material and changes in albedo alter the surface energy balance. The maturation of lunar soils results in darkening due to micrometeorite bombardment and solar wind and cosmic-ray exposure, causing the high-reflectance regions to fade with time (Lucey et al., 2000; Grier et al., 2001). Consequently bright, rayed craters are typically confined to the Copernican era (Wilhelms, 1987).

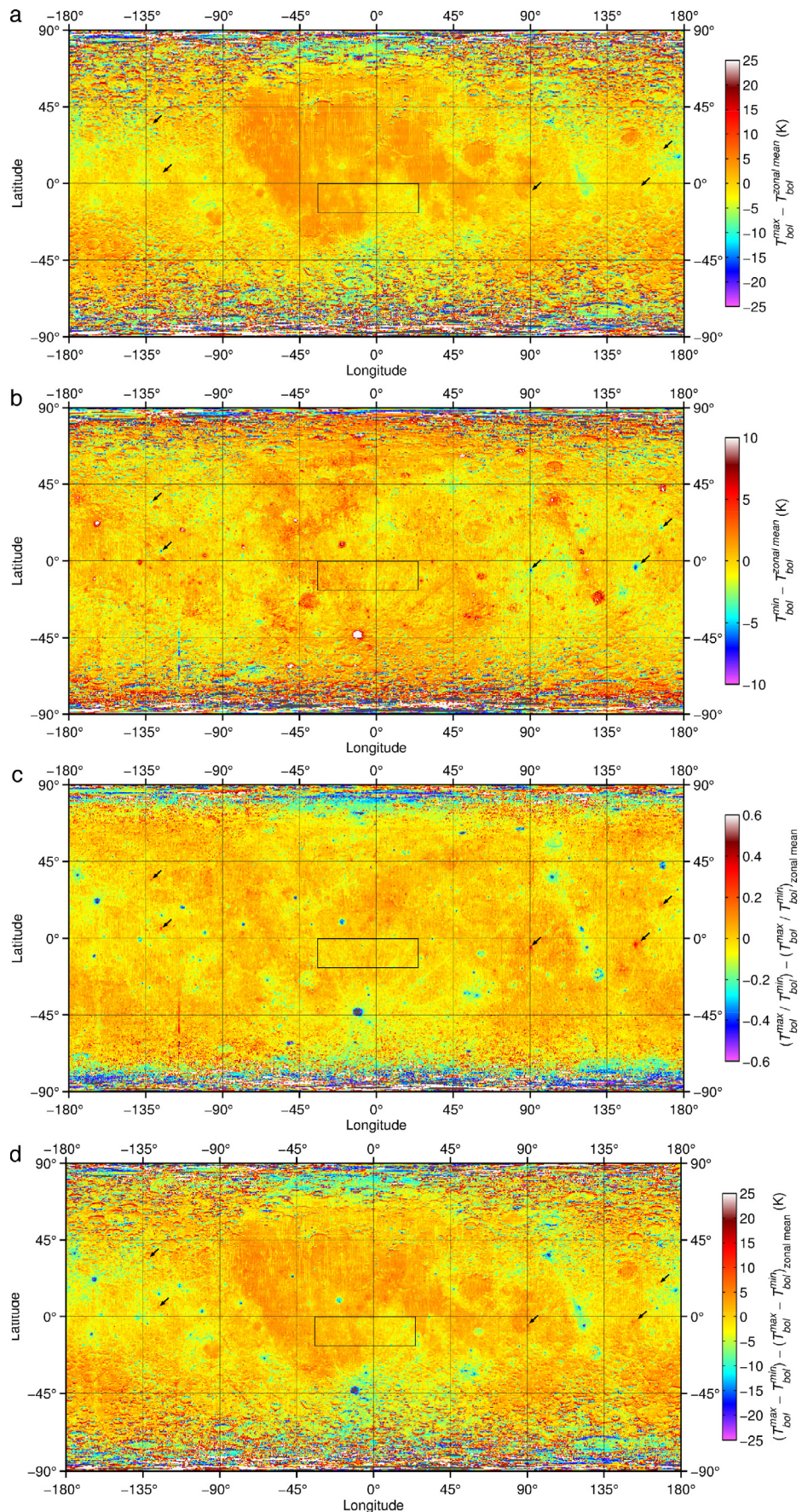


**Fig. 20.** (a) Maximum and (b) Minimum temperatures with zonal mean subtracted. (c) Ratio of maximum and minimum temperatures with ratio of the zonal mean maximum and minimum temperatures subtracted. (d) Difference of maximum and minimum temperatures with the difference of the zonal mean maximum and minimum temperatures subtracted. Arrows point to a few prominent cold spots and the black box highlights an area of fairly homogenous temperature ratio anomaly.

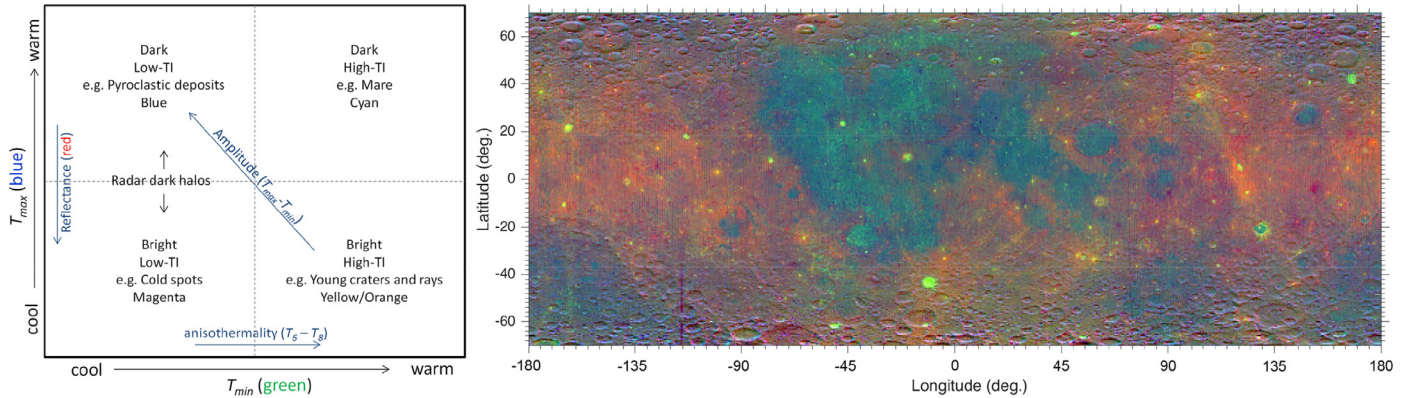


**Fig. 21.** Broad characterization of terrains based on minimum and maximum temperature anomalies. This characterization is highlighted in the RGB composite map ( $\pm 70^\circ$  latitude) where the red channel is visual brightness, the green channel is the  $T_{\min}$  anomaly, and the blue channel is the  $T_{\max}$  anomaly. Dark surfaces attain higher peak temperatures while low-TI surface attain colder minimum temperatures during the night (top left quadrant/blue). For a given  $T_{\max} - T_{\min}$  amplitude, colder  $T_{\max}$  and  $T_{\min}$  values, i.e. a shift toward the bottom left quadrant/magenta, results in higher  $T_{\max}/T_{\min}$ . The ratio can also increase with amplitude. (For interpretation of the references to colour in this figure legend, the reader is referred to the web version of this article.)

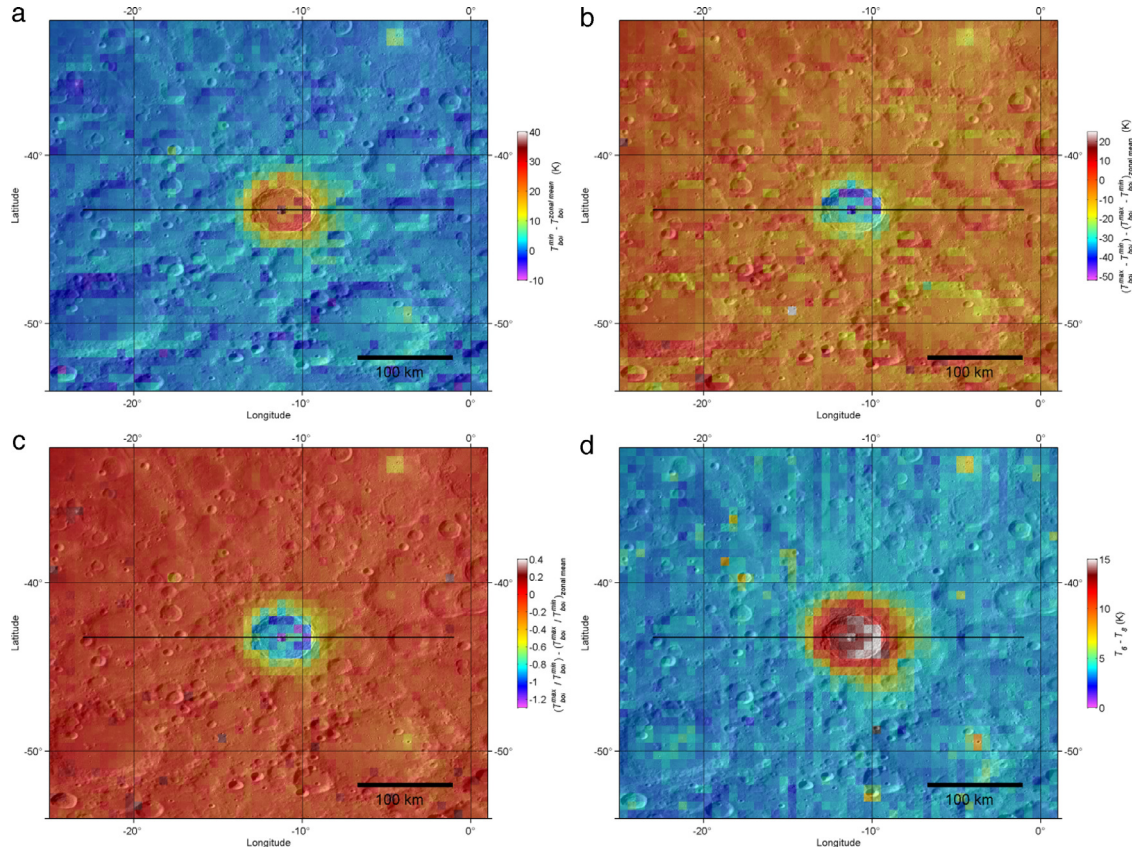


**Fig. 22.** Diviner derived maps with LRO Camera (LROC) Wide Angle Camera (WAC) mosaic shading [NASA/GSFC/ Arizona State University] centered on Tycho crater: (a) Minimum temperature anomaly, (b) maximum and minimum temperature difference anomaly, (c) maximum and minimum temperature ratio anomaly, and (d) Diviner channel 6 and 8 nighttime anisothermality. Black line is the ground track of profiles in Fig. 23.

### 5.1.1. Tycho crater

Tycho crater ( $43.3^\circ\text{S}$ ,  $11.4^\circ\text{W}$ ) represents one of the most significant thermal anomalies in nighttime IR observations (Figs. 22, 23) and displays some of the most extensive rays visible on the Moon (Figs. 24, 25). With a diameter of 86 km and an estimated age  $\sim 100$  Ma (Drozd et al., 1977; Stöffler and Ryder, 2001; Hiesinger et al., 2012), Tycho is the youngest crater of its size with Copernicus,  $\sim 800$  Ma (Eberhardt et al., 1973; Alexander et al., 1976), being the only Copernican-age crater larger ( $D \sim 93$  km). The crater interior and surrounding areas have a relatively high reflectance

relative to the highland terrain (Fig. 22a) resulting from the exposure of immature materials. Tycho's interior and rim are associated with high optical maturity parameter (OMAT) values (Grier et al., 2001). An annulus, approximately one crater radius thick, of reduced reflectance exterior to the rim is observed in the Diviner visible brightness data. This halo results from a torus of optically dark impact melt glass surrounding the crater (Hawke et al., 1979). The more distal, bright surfaces are distributed to a greater extent to the east, along with a greater prominence of rays (Fig. 24) consistent with an oblique impactor coming generally from the west.

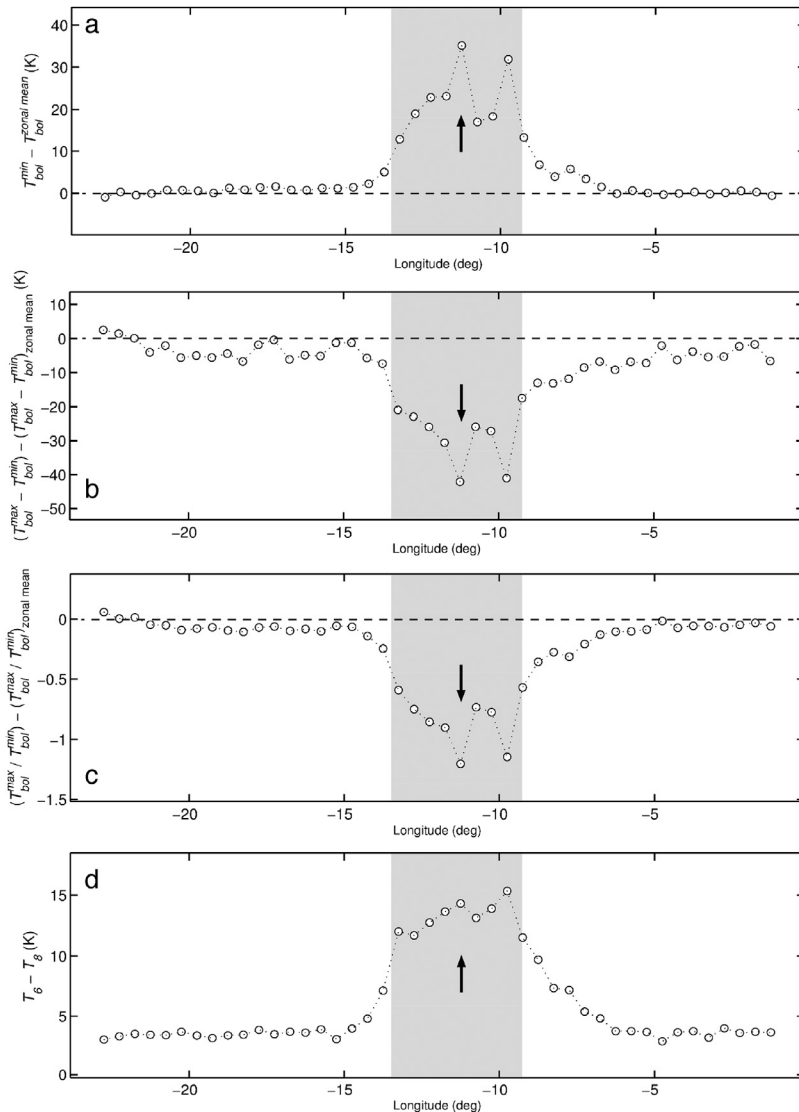


**Fig. 23.** Profiles (west-east) across Tycho crater from Fig. 22. (a) Minimum temperature anomaly, (b) maximum and minimum temperature difference anomaly, (c) maximum and minimum temperature ratio anomaly, and (d) Diviner channel 6 and 8 nighttime anisothermality. Gray shading corresponds to the crater interior (rim-to-rim) and the black arrow points to the location of the crater's central peak.

This distribution is also apparent in the higher than average emissivity contrast between Diviner channels 4 and 7 associated with the high-reflectance immature material around Tycho (Fig. 13).

The rim and interior of Tycho have some of the warmest nighttime temperatures with minimum temperatures of the central peak and eastern wall exceeding the zonally averaged minimum temperatures by >30 K (Figs. 22a, 23 a). This is primarily the result of the fresh, rocky interior containing impact melt and large blocks and boulders though thermal emission from the walls and floor may contribute to warming adjacent surfaces. Maximum daytime temperatures within the region of Tycho are generally reduced due to the high-reflectance surface, though at a latitude >40°, there is substantial variation in temperatures between north and south facing slopes. The mean maximum temperature anomaly for a 10° × 10° region centered on Tycho crater is −3.53 K. An east-west profile of the moving average of the 10° × 10° region in 5° increments of longitude, show the reduction in average peak temperatures in the vicinity of Tycho (Fig. 26). The minimum of the profile however is not centered on Tycho, but offset to the east consistent with the observation of high-reflectance surfaces extending further from the crater toward the east.

The maximum-minimum difference reflects the smaller temperature amplitudes experienced by the poleward facing slopes compared with the equator facing slopes through a lunation (Fig. 22b). The  $T_{max} - T_{min}$  of the north wall of Tycho is ~35–45 K smaller than the average for that latitude, while for the equator facing wall it is ~20–25 K smaller. The relative temperature difference however ( $T_{max}/T_{min}$ ) is less sensitive to slope effects (as discussed in Section 4) and shows an east-west asymmetry in the relative temperature differences (Fig. 22c). This results from the warmer minimum temperatures on the eastern wall. The asymmetry cannot be entirely attributed to the western wall being in shadow in the afternoon as nighttime anisothermality shows a strong east-west asymmetry as well (Fig. 22d). The nighttime  $T_6 - T_8$  anisothermality is sensitive to mixtures of warmer and cooler temperatures within Diviner's field-of-view (e.g. Williams et al., 2016). The strongest anisothermality occurs along the eastern crater wall and central peak indicating a greater abundance of warmer high thermal inertia materials.

The east-west asymmetry can be seen in profiles across Tycho (Fig. 23). Peak minimum temperatures and anisothermality occur on the eastern wall and central peak while the absolute and

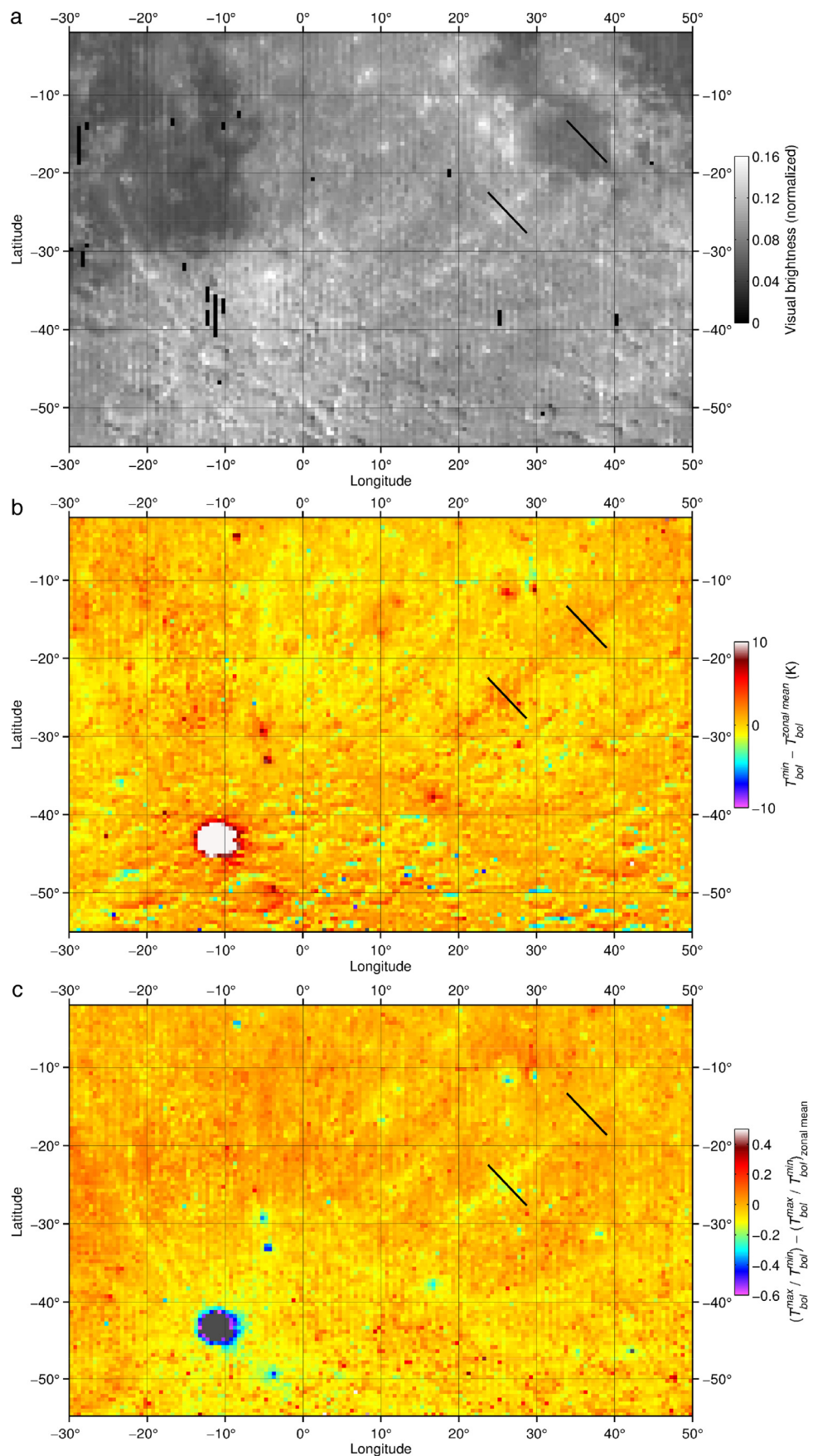


**Fig. 24.** Portion of Diviner global maps highlighting Tycho crater and rays. (a) Diviner channel 1 visible brightness photometrically normalized by latitude. (b) Minimum temperature anomalies. (c) The ratio of maximum and minimum temperature anomalies. The two black lines show locations of the profiles in Fig. 25 in the highlands and Mare Nectaris at distances of 1062 km and 1496 km from Tycho respectively.

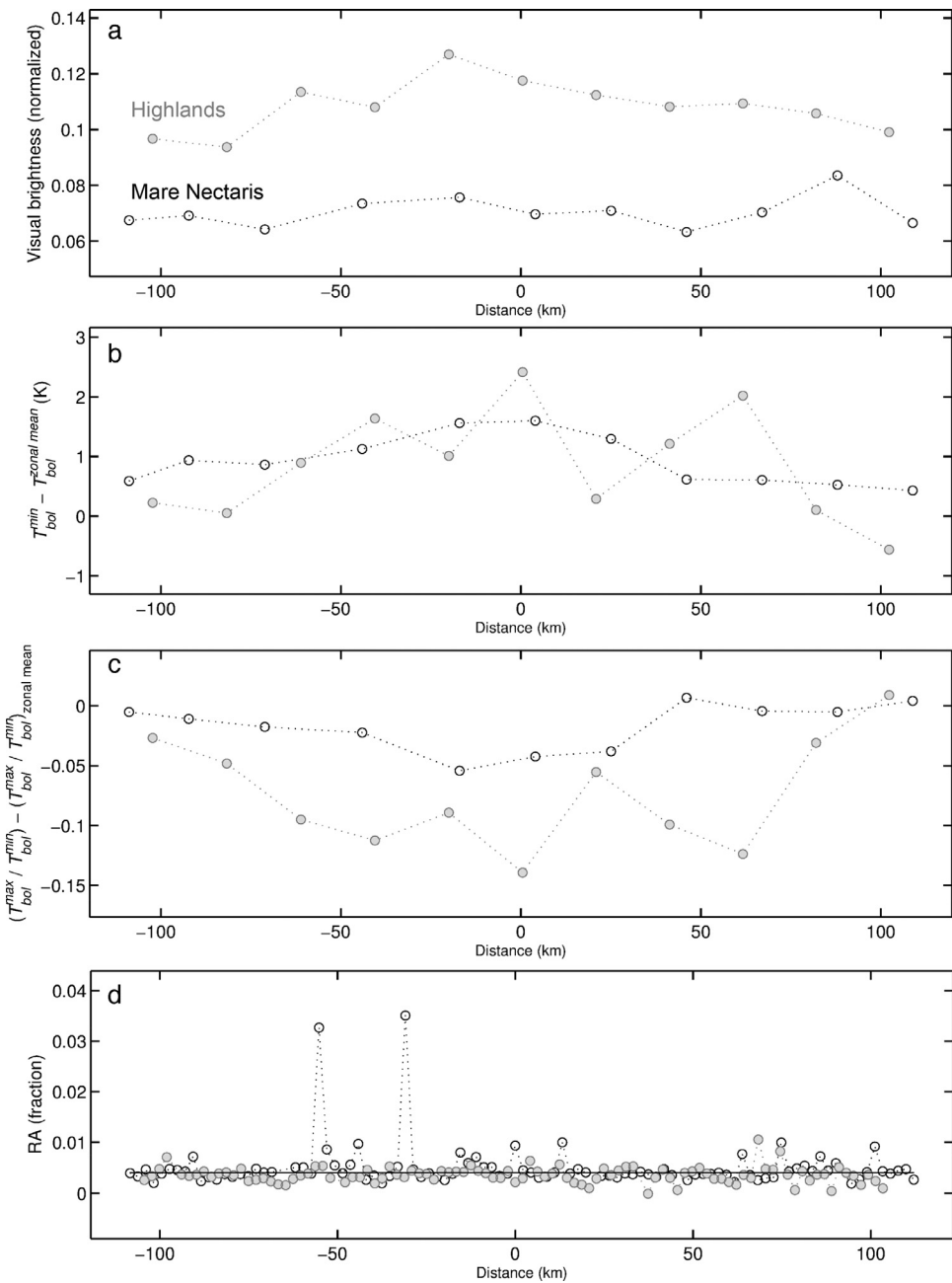


**Fig. 25.** Profiles through a Tycho ray at a distance of 1062 km and 1496 km. (a) Channel 1 visual brightness, (b) minimum temperature anomaly, (c) maximum/minimum ratio anomaly, and (d) rock abundance at 128 ppm (Bandfield et al., 2011). The minimum temperatures are higher in the ray and  $T_{max}/T_{min}$  is reduced consistent with a brighter, higher thermal inertia surface, however rock abundance is relatively uniform with the exception of rocky craters within the mare indicating the thermal contrast of the ray must result from predominately small ( $\lesssim 0.5$  m) objects.

relative temperature differences are at minimums at these locations. An asymmetry in thermal properties is also observed exterior to the crater where thermal properties trend back to background levels over a larger distance east of the crater. Background levels occur within  $\sim 2^\circ$  longitude west of the crater but  $\sim 4^\circ$  longitude to the east consistent with the impact influencing the regolith properties to a greater extent to the east. This further indicates the east-west asymmetry is not a result of differences between morning and afternoon illumination conditions.

The Diviner observations are consistent with an oblique impact from a general west direction for Tycho. This is consistent with the greater distribution of impact melt deposits on the eastern ejecta (Morris et al., 2000; Krüger et al., 2013), and the azimuthal asymmetries in: (1) the crater wall and rim topography (Krüger

et al., 2013), (2) continuous ejecta blanket and immature material observable in OMAT values (Hirata et al., 2004), and (3) secondary impact crater densities and rays (Dundas and McEwen, 2007).

#### 5.1.2. Crater rays

Crater rays are most easily seen at optical wavelengths, however, the more prominent rays are observed by Diviner even at the coarse  $0.5 \text{ deg pix}^{-1}$  resolution of these global maps. Rays are attributed to either a compositional contrast with surrounding terrain, the presence of immature materials, or both as a result of the emplacement of primary ejecta materials or processes related to secondary cratering (Hawke et al., 2004). Rays observed as thermal anomalies in nighttime temperatures however result from contrasting thermophysical properties. Figs. 24 and

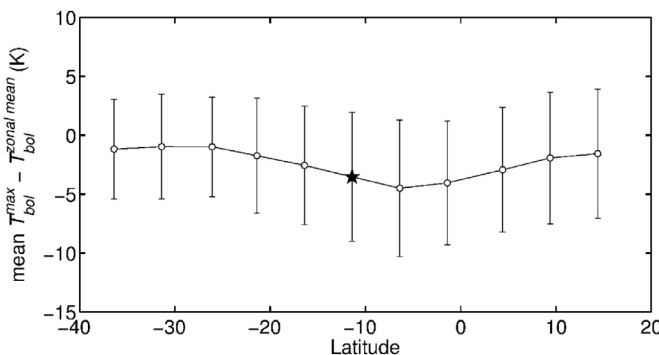


**Fig. 26.** The moving average of the maximum temperature anomalies for a  $10^\circ \times 10^\circ$  box aligned with the center latitude of Tycho crater ( $43.3^\circ\text{S}$ ) shifted in  $5^\circ$  longitude increments. The black star corresponds to the  $10^\circ \times 10^\circ$  box aligned with Tycho's center ( $11.4^\circ\text{W}$ ). Error bars are the standard deviation.

25 highlight one of the more prominent rays of Tycho extending  $\sim 2000$  km northeast to about  $48^\circ\text{E}$ ,  $5^\circ\text{S}$  with a variable width typically  $\sim 100$  km. Profiles of visual brightness,  $T_{min}$  anomaly, and  $T_{max}/T_{min}$  anomaly are shown in Fig. 25 where the ray crosses both highland terrain and Mare Nectaris. Nearly the entire  $\sim 2000$  km length of the ray has warmer minimum temperatures than the adjacent terrain indicating the presence of material with higher thermal inertia than the nominal regolith. The ray also displays a depression in the ratio of maximum to minimum temperatures indicating the relative change in temperatures experienced by the ray is less than both the highland and maria regolith.

Bandfield et al. (2011) modeled mixtures of rock abundance and regolith fines temperatures using Diviner data. The rock abundance estimates do not show an enhancement of rock concentration in the ray. The thermal skin depth for a basaltic rock under lunar diurnal conditions is  $\sim 0.5\text{--}1$  m indicating the thermal contrast in the minimum temperatures observed in the ray must largely result from objects primarily smaller than this size. The modeled regolith fines temperatures do show an enhancement consistent with the fine component within the ray being thermally anomalous. There is an inherent size dependence on the nighttime thermal signature of rocks as smaller rocks will cool more rapidly. This is observed in the rock abundance as the retrieved rock concentrations diminish throughout the night. The fact that we still see a temperature anomaly at the minimum temperatures corresponding to just before sunrise, indicates that material within the ray remains anomalously warm for the duration of the lunar night. This ray is also observed to be radar bright (Zisk et al., 1974; Campbell et al., 1992; Neish et al., 2013) implying a difference in physical properties within the ray caused by radar scatterers such as rocks with sizes comparable to the wavelength of radar at or near the surface. A correlation between radar bright surfaces in X-Band (3.8 cm) and the high-albedo portions of the ray, but not P-Band (70 cm), indicates scattering is due to 1–50 cm fragments, but not larger (Neish et al., 2013). This is consistent with Diviner observations indicating a greater abundance of small rocks within the ray and precludes formation by a dusting of very fine material with minimal disruption to the target surface.

## 5.2. Fine grain deposits – pyroclastic and radar dark materials

Numerous pyroclastic deposits have been identified on the Moon (Gaddis et al., 1985; 2003; Weitz et al., 1998; Gustafson et al., 2012). Several of the most areal extensive deposits are in the vicinity of Mare Vaporum (Fig. 27) where deposits mantle mare and highland surfaces to form low albedo regions observable in the Diviner maps. In addition to having lower than typical emissivity differences between the Diviner 4 and 7 passbands

(Section 4.2.1; Fig. 13) due to compositional differences, they experience warmer peak temperatures and colder minimum temperatures than the nominal regolith due to their low reflectivity and low thermal inertia. This is shown in Fig. 27 where the dark regional deposits have anomalously low  $T_{min}$  and larger  $T_{max}/T_{min}$ . This is the opposite to the bright, rocky interior and rim of Copernicus crater also visible in Fig. 27.

The low minimum temperatures of these regions indicate they are blanketed by largely fine-grained and rock free mantling deposits, consistent with the low  $T_6-T_8$  anisothermality observed by Diviner (Fig. 27d) and low radar returns requiring an absence of surface scatterers in the 1- to 50 cm-size range (Gaddis et al., 1985). The deposits are interpreted as the products of explosively emplaced pyroclastic eruptions (Head, 1974) comprised of glass beads with differing degrees of crystallinity and finely fractured basalt (Gaddis et al., 2003).

Haloes of low  $T_6-T_8$  nighttime anisothermality are also apparent around the crater Copernicus and other impact craters (Fig. 27d) indicating an annulus of more homogenized material depleted in surface rocks around the craters. These correspond to “radar-dark” haloes (Thompson et al., 1970, 1974; Ghent et al., 2005), regions of low radar backscatter and low circular polarization ratios consistent with fine-grained, rock-poor material. Haloes of relatively uniform nighttime temperatures comparable or lower than surrounding mare plains were also observed around larger craters in Apollo 17 Scanning Infrared Radiometer experiment data (Schultz and Mendell, 1978). Ghent et al. (2016) concluded that these are distal ejecta deposits of fairly uniform thickness 10–30 m thick and unlike the pyroclastic deposits, the bolometric temperatures are thermally indistinct from nominal regolith. We do find that the elevated minimum temperatures throughout Mare Imbrium are subdued in the locations corresponding to the crater annuli of low anisothermality with minimum temperature anomalies  $\sim 0$  K (Fig. 27b), consistent with material having thermophysical properties similar to nominal regolith. The interpretation of radar-dark halos as rock-poor material with similar thermophysical properties to nominal regolith fines material (Ghent et al., 2016) is consistent with the Diviner observations of low anisothermality haloes indicating material of greater homogeneity without distinctive minimum temperatures.

## 5.3. Orientale basin

The 930 km diameter Orientale basin, located on the western limb of the Moon ( $19^\circ\text{S}$ ,  $93^\circ\text{W}$ ), is the youngest and most well-preserved of the large multi-ringed lunar impact basins (e.g. Head, 1974; Spudis et al., 1984, 2014; Whitten et al., 2011) estimated to have formed during the Late Imbrium period (Wilhelms, 1987). The basin is not significantly filled with mare basalts and its interior and ring structures remain largely exposed unlike other lunar impact basins. Basin-forming impacts like Orientale redistribute a significant volume of the crust modifying large portions of the lunar surface in a geologic instant.

The thermal signature of the Orientale basin (Fig. 28) demonstrates the widespread influence the impact event has had on the regolith and megaregolith properties in the western hemisphere. The basin itself, defined by the outermost Cordillera ring, covers an area of  $\sim 700,000$  km $^2$ . Volcanic activity within the basin occurred over a significant time period ( $\sim 1.9$  Ga) with the earliest, most voluminous emplacement of basalt forming Mare Orientale at the basin center (Greeley et al., 1993). Despite the protracted period of volcanism, the total estimated volume of basalt,  $\sim 46,000$  km $^3$ , is much smaller than typical of nearside impact basins (Whitten et al., 2011). The mare deposits within the interior of the basin are the most thermally distinct surfaces in daytime temperatures due to their low reflectivity (Fig. 28a) with anomalously warm peak

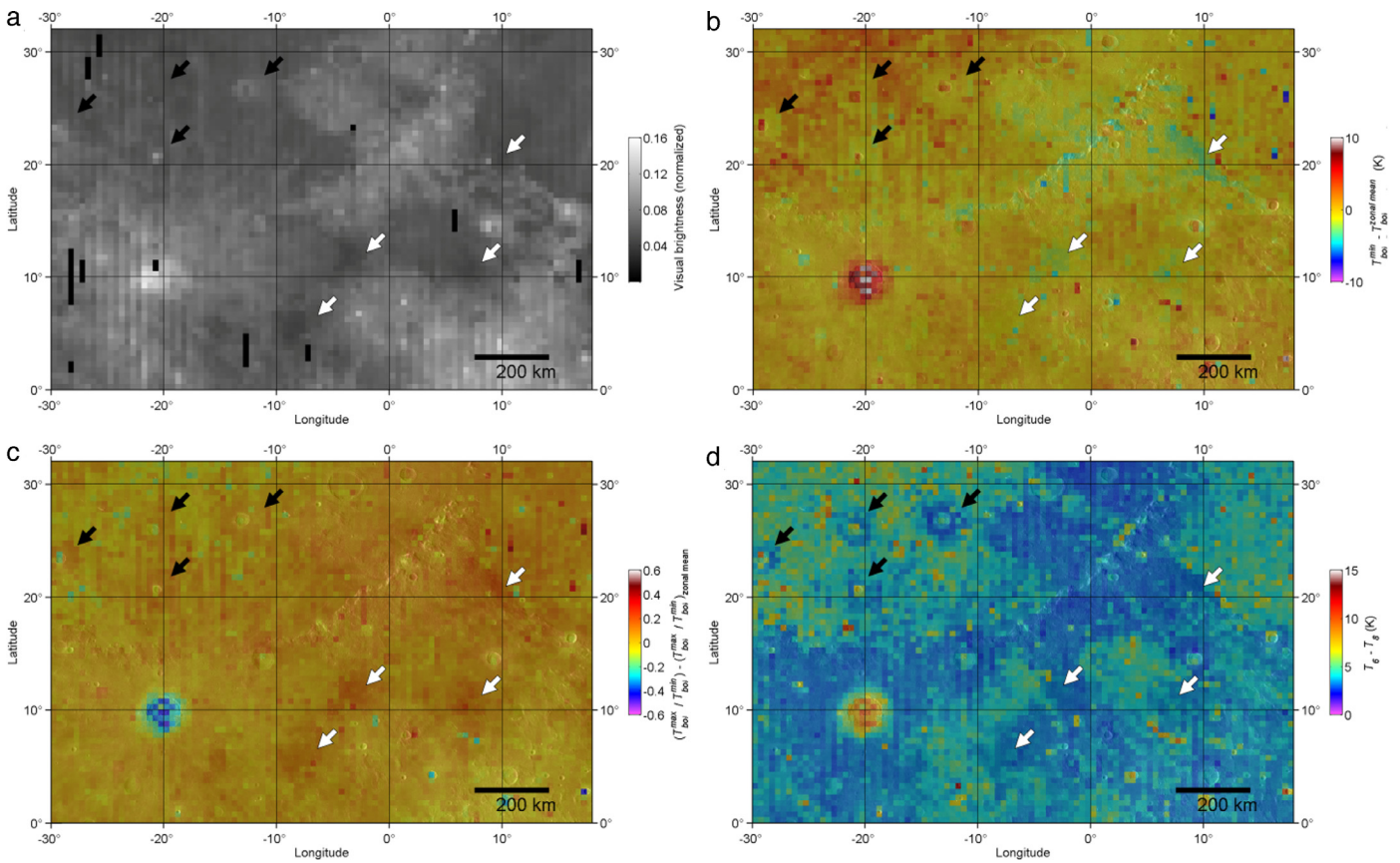


**Fig. 27.** Portion of Diviner global maps: (a) Diviner channel 1 visible brightness photometrically normalized by latitude, (b) minimum temperature anomalies, (c) the ratio of maximum and minimum temperature anomalies, and (d) Diviner channel 6 and 8 nighttime anisothermality. Mare Imbrium is in the top left portion of the figures and Copernicus crater is the high albedo circular feature in the lower left of (a). White arrows point to large pyroclastic deposits (from east to west): Sulpicius Gallus, Vaporum, Rima Bode, south Sinus Aestuum. Black arrows highlight, in addition to Copernicus crater, smaller craters with radar-dark haloes in Mare Imbrium.

temperatures similar to mare deposits in Oceanus Procellarum and other nearside basins (Fig. 28c). Anomalously cool daytime temperatures within the basin interior are associated with scarps on the Inner and Outer Rook rings or radial elongate ridges within the basin, predominately in the western half of the basin.

The warmest minimum temperatures are associated with a lobe of the Montes Rook Formation that extends beyond the Cordillera scarp in the southwest corner. The Montes Rook Fm. is elsewhere restricted to the basin interior and has been suggested by Spudis et al. (2014) to be at least partially composed of impact melt based on the observed presence of flow lobes. The elevated minimum temperatures are suggestive of higher thermal inertia material. This area also corresponds to higher  $T_6-T_8$  nighttime anisothermality indicative of elevated concentrations of rocks (Figs. 28b, 29) consistent with the presence of impact melt. Elevated anisothermality is also associated with the Inner and Outer Rook scarps and superposed craters and is predominately confined to the western half of the basin. The average radar backscatter observed by the Mini-RF instrument (Nozette et al., 2010) is also higher in the western half of the basin (Cahill et al., 2011).

Deposits exterior to the basin are collectively named the Hevelius Formation (Scott et al., 1977). The inner facies are comprised of continuous deposits forming an annulus of material ~300–600 km wide (Wilhelms, 1987). Fassett et al. (2011) estimate a deposit thickness of ~2.9 km near the Cordillera scarp decaying to ~1 km at a distance of 215 km. The outer facies, at ranges beyond the continuous deposit, transitions into discontinuous units including smooth plains and secondary craters with many

prominent crater chains oriented radial to the basin. The continuous deposits of the inner facies are discernible in Diviner data as a region of relatively uniform, low  $T_6-T_8$  nighttime anisothermality from the Cordillera ring extending radially outward to a digitate outer margin that roughly corresponds to the contact mapped by Scott et al. (1977). This annulus of low anisothermality, most prominent in the south and east, is also found to be a region of low radar return (Ghent et al., 2008; Cahill et al., 2011, 2014) implying the unit is related to radar-dark halos observed around other sizeable craters (Section 5.2) with an absence of rocks at or near the surface. Mini-RF has revealed the western portion of the annulus to have higher radar return relative to the east (Cahill et al., 2014).

Beyond this annulus of material, streaks of enhanced radar return oriented radial to Orientale extend >2700 km from the basin center (Ghent et al., 2008). Enhanced anisothermality in radial patterns are observed to distances of ~1600 km from the basin center with the most prominent signature in the southeast in the Schiller-Schickard region, a region associated with cryptomaria, mare deposits covered by lighter plains deposits (Head and Wilson, 1992; Blewett et al., 1995; Whitten and Head, 2015).

Bandfield et al. (2016) have identified a diffuse distribution of anomalously elevated rock abundances within a ~730,000 km<sup>2</sup> area centered within this region. The elevated rock abundances are associated with the occurrence of isolated rubble piles and granular flow deposits on crater walls preferentially found on west and northwest-facing slopes. It is possible that the granular flows were triggered by the emplacement of the blocks. Such elevated rock concentrations are rare within the lunar highlands and are

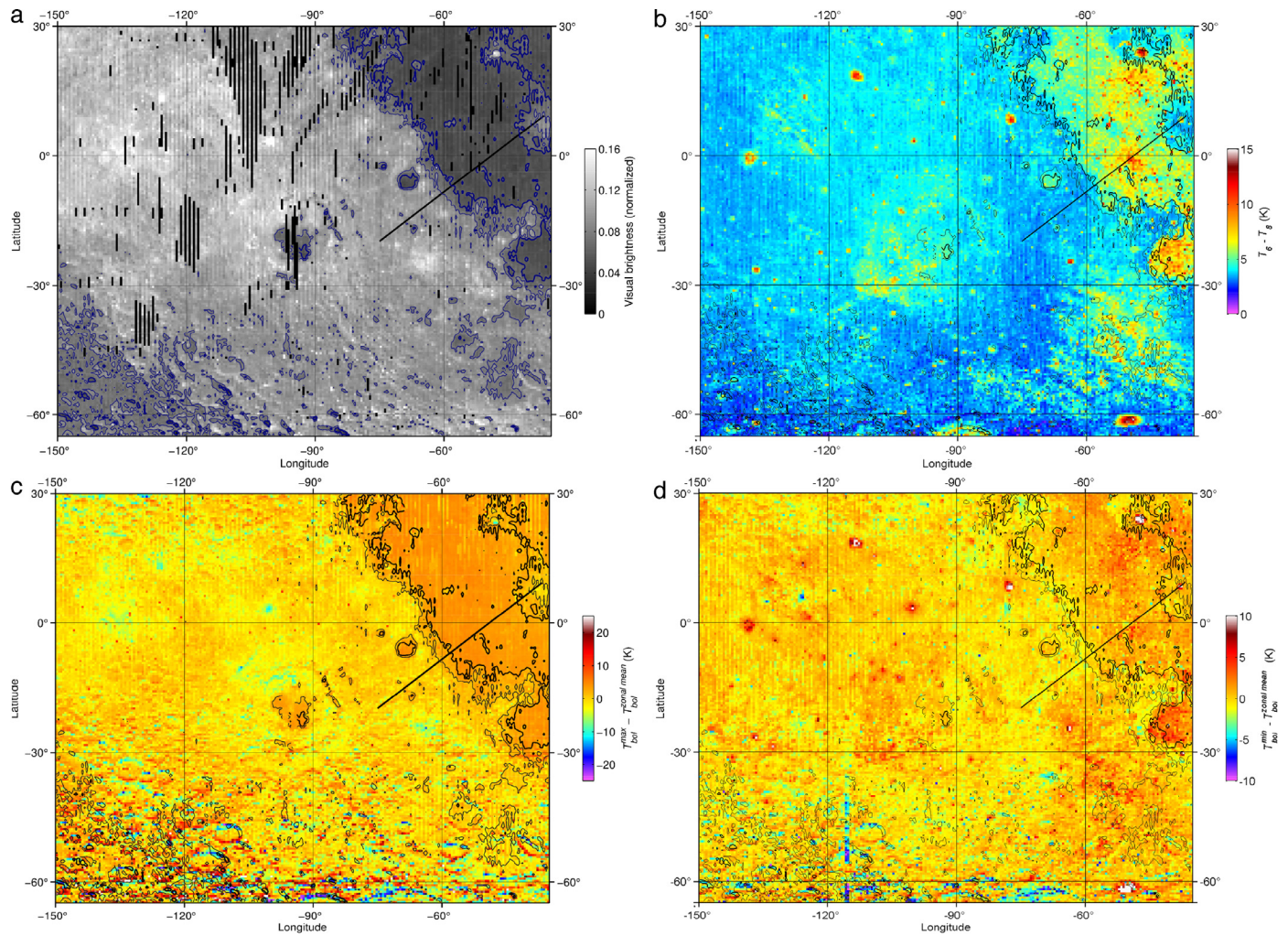


**Fig. 28.** Diviner maps of Orientale and southwest Oceanus Procellarum region: (a) Diviner channel 1 visual brightness photometrically normalized by latitude, (b) Diviner channels 6 – 8 nighttime anisothermality, (c) Maximum temperature anomaly, and (d) Minimum temperature anomaly. Thick contour is visual brightness level 0.06 and thin contour is the 0.08 level. Black line is the location of profiles in Fig. 30.

typically associated with Copernican-age surfaces as the comminution of blocks is fairly rapid (Bandfield et al., 2011; Ghent et al., 2014). It is unlikely therefore that these elevated rock abundances identified by Bandfield et al. (2016) are directly related to the Orientale impact event and require a more recent, Copernican-age, event. Orientale deposits, however likely altered the megaregolith properties of the western hemisphere in a way that could influence the resulting thermal signatures of more recent events. This is analogous to the mare appearing rocky in the Diviner nighttime temperatures relative to the highlands. Diviner does not detect the competent, intact basalt flows directly, but rather the high density of small craters that excavate meter-scale rocks from underneath a thinner than average regolith layer overlying the basalt flows. The anomalous  $T_6-T_8$  nighttime anisothermality associated with the sizeable melt deposit on the southwest margin of the Orientale basin (Fig. 29) is evidence for the continued influence that Orientale has on the regolith and megaregolith properties. It is unusual for the thermal signature of melt deposits to persist much beyond the Copernican period (Ghent et al., 2014), though the farside crater Tsiolkovskiy, with an age > 3 Ga (Williams et al., 2013), is another conspicuous exception with a prominent elevated rock abundance signature associated with a large impact melt deposit exterior to its southern rim (Greenhagen et al., 2016). In the case of Tsiolkovskiy, the magnitude of the rock abundance is

higher than contemporary equivalents, which may be evidence for a large-scale surface modification event during the Copernican age.

#### 5.4. Oceanus procellarum

The mare-highland boundary of south-western Oceanus Procellarum was likely modified by the Orientale impact event. Cryptomare has been identified in the region between Procellarum and the Orientale basin (Hawke et al., 1993; Mustard and Head, 1996; Campbell and Hawke, 2005; Whitten and Head, 2015) indicating pre-Orientale mare deposits were established in the region prior to the formation of the basin and radar and multispectral analysis have shown the western margin of Procellarum to be a complex mixture of mare and highland terrain. Using earth-based 70 cm wavelength radar images, Campbell and Hawke (2005) conclude that mare basalt, or a mixture of mare and highland material, exists at depth across the region only reaching the visible surface near the margin of western Procellarum. A profile from the Diviner maps across this region, shown in Fig. 30, extends from within the inner Hevelius Fm., across the mare-highland boundary between Cruger and Grimaldi craters, to Kepler crater within Oceanus Procellarum. Mustard and Head (1996) found the mare abundance across the mare-highland contact in this location

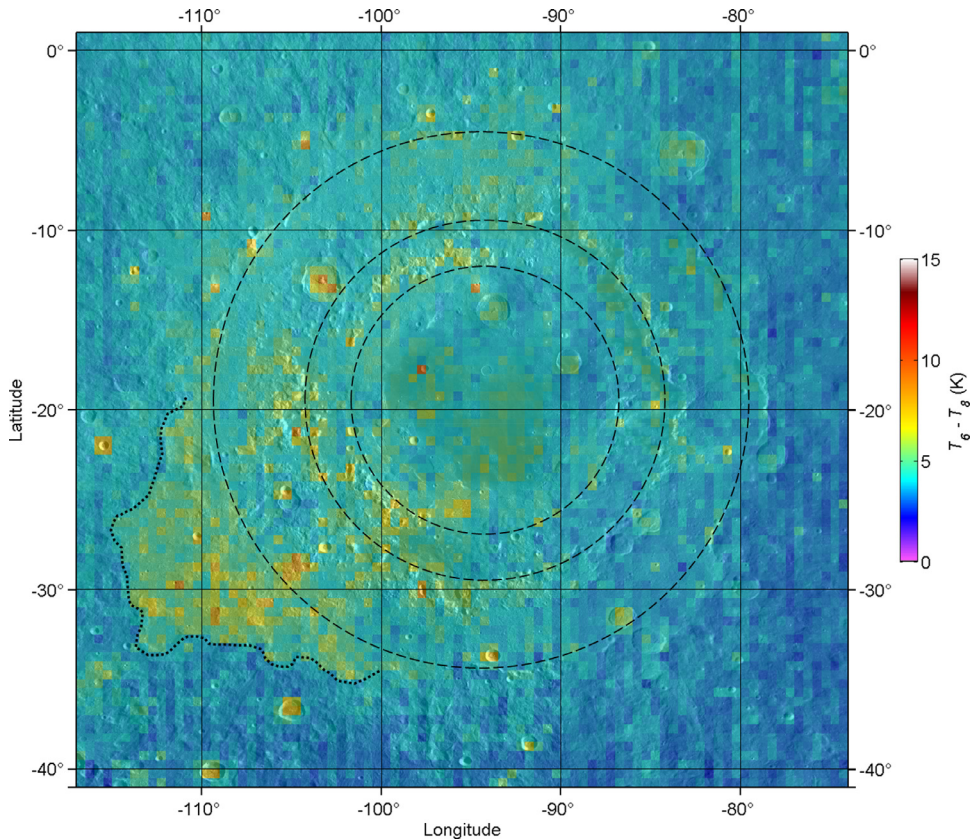


**Fig. 29.** Diviner channels 6 – 8 nighttime anisothermality with LROC WAC mosaic shading centered on Orientale Basin. The approximate locations of the Inner Rook, Outer Rook, and Cordillera rings are outlined by dashed circles. The extent of the elevated anisothermality exterior to the Cordillera scarp is outlined with a dotted line which corresponds to the Montes Rook Fm. contact mapped by Spudis et al. (2014).

to be gradational over a  $\sim 100$  km zone with the geologic contact on the high mare side of the mixing gradient.

Diviner visual brightness (Fig. 30a) shows a gradation in reflectance over a distance of  $\sim 200$  km across the mare-highland boundary. Maximum temperatures also increase over this same region as a result of the gradient in radiative properties. In contrast, the gradient in thermophysical properties (e.g.  $T_6-T_8$  nighttime anisothermality and minimum temperature anomaly; Fig. 30b,d) appears relatively narrow and abrupt by comparison (within one or two map pixels,  $\sim 20$ – $40$  km) and occurs at the low side of the visual brightness gradient at  $\sim 0.06$ . Mustard and Head (1996) argue that the broad compositional mixing zone observed in multispectral data, consistent with the broad gradient in reflectance observed by Diviner, precludes a relatively simple stratigraphic relationship because physical mixing of materials at compositional boundaries by vertical and lateral transport via impacts and regolith gardening is limited. Based on the observed broad gradient in composition, and evidence for cryptomaria in the region, it has been suggested that basin ejecta from the Orientale event mixed with pre-existing, proto-Procellarum basalts (Mustard and Head, 1996; Campbell and Hawke, 2005).

Diviner does see a similarly broad gradient in reflectance at Kepler crater within the interior of Procellarum corresponding to the visible, bright ejecta superposed on the mare. There is also a reduction in  $T_6-T_8$  nighttime anisothermality and minimum temperature anomaly across this gradient corresponding to the radar-dark halo with an abrupt transition in thermophysical properties near the crater rim. This highlights how impacts can modify the radiative and thermophysical properties of the surface and near-surface layer over large distances ( $> 10$  crater radii).

## 6. Summary

We have generated a global dataset from the compilation of nearly six years of accumulated calibrated radiance measurements by Diviner providing a comprehensive view of the thermal state of the near-surface layer of the moon at  $0.5^\circ$  resolution. The lunar thermal environment is extreme. Daytime temperatures are in near-radiative equilibrium with noontime temperatures  $\sim 387$ – $397$  K at the equator, dropping  $\sim 300$  K to around 95 K just before sunrise. In comparison, the average maximum temperature in the polar regions (poleward of  $85^\circ$ ) is  $\sim 200$  K with average minimum temperatures  $\sim 50$  K, though the south polar region has an average maximum temperature  $\sim 11$  K warmer than the north polar region. An asymmetry is observed between the morning and afternoon temperatures due to the thermal inertia of the lunar regolith resulting in a lag between heating and cooling of the regolith. This is most apparent at high incidence angles with the dusk terminator  $\sim 30$  K warmer than the dawn terminator at the equator.

We find that the decrease in temperatures with incidence angle require an increasing albedo with incidence angle consistent with previous Diviner observations (Vasavada et al., 2012). Surface roughness and topography results in increasing variability in temperatures above  $\sim 40^\circ$  incidence angles, toward high latitudes and the terminators. Anisothermality in the Diviner channels also increase at high incidence angles due to increasing slope effects and shadows within the instrument's field of view. At low incidence angles ( $\lesssim 30^\circ$ ) differences in brightness daytime temperatures between Diviner channels are due to different emissivities in the spectral passbands of the channels. Mapping of low-incidence angle anisothermality shows variations that correlate with compositional differences.

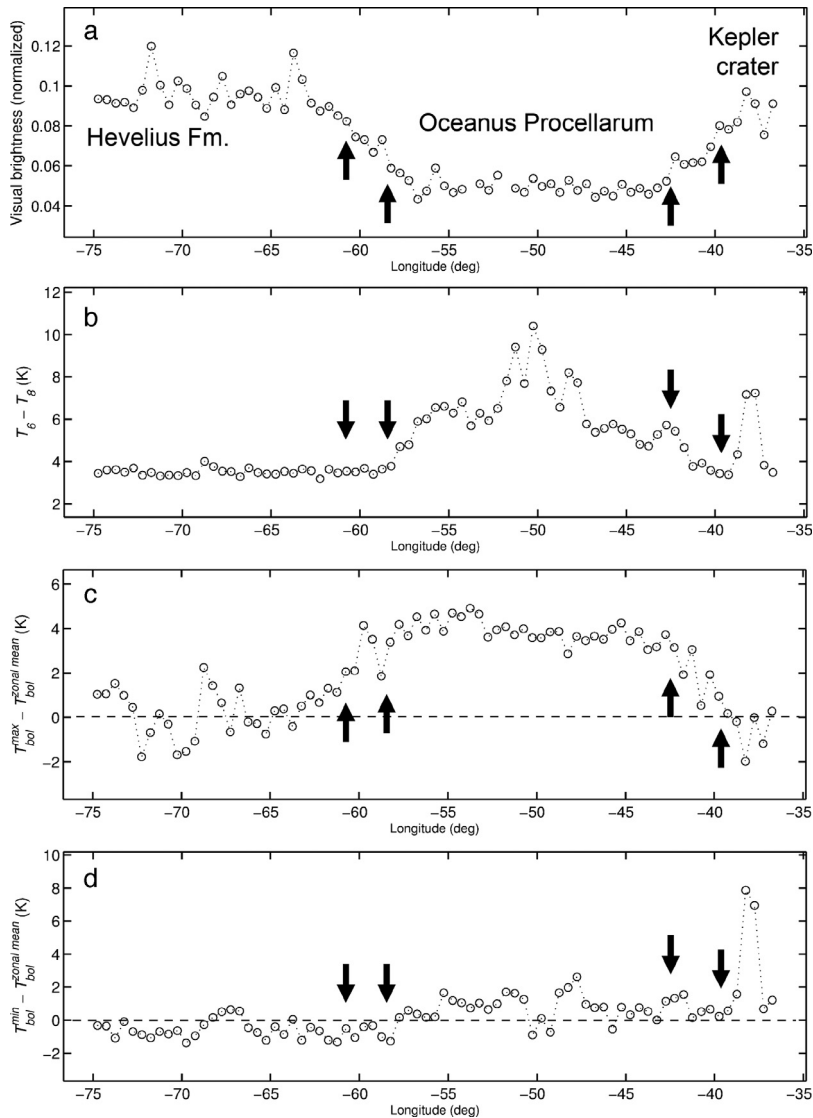


**Fig. 30.** Profiles from the Diviner maps in Fig. 28 of (a) normalized visual brightness, (b)  $T_6 - T_8$  nighttime anisothermality, (c) Maximum temperature anomaly, and (d) Minimum temperature anomaly. Arrows correspond to locations of the 0.06 and 0.08 visual brightness contours in Fig. 28. The dash horizontal lines highlight the zero values for clarity in (c) and (d).

Nighttime temperatures are sensitive to the thermophysical properties of the regolith. Subtracting the zonal mean nighttime temperatures from nighttime temperature maps reveals the global pattern of varying nighttime surface temperatures. Anisothermality between the longer wavelength Diviner channels in nighttime temperatures further highlights variations in thermophysical properties. The coldest nighttime surfaces are associated with lunar cold spots (Bandfield et al., 2014), highly insulating regions around very young craters extending  $\sim 10\text{--}100$  crater radii. The three largest cold spots have surfaces that remain  $> 5\text{ K}$  colder than mean zonal temperatures and maintain this temperature difference throughout the night. The warmest nighttime temperatures correspond to bright-rayed Copernican-age craters. The warmest average nighttime temperature,  $\sim 50\text{ K}$  higher than the zonal average, is associated with a portion of the crater Giordano Bruno. Unlike the cold spots, the thermal contrast of the rocky craters diminishes through the lunar night.

The relative and absolute differences between the mapped maximum and minimum temperatures provides a useful metric for identifying and mapping terrain variations, as these values are sensitive to both radiative and thermophysical properties. This

allows terrains to be characterized as high- or low-reflectance and high- or low-thermal inertia. The thermal signature of Tycho crater is asymmetric with high reflectance, and higher thermal inertia material distributed to a greater extent eastward of the crater rim and at a higher abundance on its eastern interior wall, consistent with an oblique impact coming from the west. Crater rays are observed by Diviner and several are resolved in the  $0.5^\circ$  maps. The most prominent ray from Tycho requires material with higher thermal inertia than nominal regolith with rocky fragments at the surface  $< 50\text{ cm}$  in size. Regions of fine-grained materials are conspicuous in the Diviner maps and include dark, pyroclastic deposits and “radar-dark” haloes around craters.

Orientale basin has influenced the thermal properties of the regolith and megaregolith over a significant portion of the western hemisphere. This thermophysical modification extends much further spatially than is apparent in the albedo and includes a prominent melt deposit extending beyond its southwest rim, an extensive halo of rock-poor material corresponding to a radar-dark region, and radially oriented patterns of elevated anisothermality extending to distances of  $\sim 1600\text{ km}$  from the basin center. The mare-highland boundary of southwest Oceanus

Procellarum consists of a broad ~200 km gradient in reflectance consistent with the suggestion that basin ejecta from Orientale mixed with pre-Orientale mare in the region between Procellarum and Orientale. The gradient in thermophysical properties across the mare-highland contact in contrast, is abrupt (~20–40 km). Similarly broad and narrow gradients in reflectance and thermophysical properties are observed around other craters like Kepler, demonstrating how impacts can modify regolith properties over large distances (>10 crater radii).

## Acknowledgements

We thank the LRO Diviner operations team for their effort in returning the data presented here and Paul Hayne and an anonymous reviewer for helpful discussion and feedback. This work was supported by the LRO project and the Diviner science investigation, under contract with NASA.

## References

- Alexander Jr., E.C., Bates, A., Coscio Jr., M.R., Dragon, J.C., Murthy, V.R., Pepin, R.O., Venkatesan, T.R., 1976. K/Ar dating of lunar soils ii. In: *Proc. 7th Lunar Sci. Conf.* 7, pp. 625–648.
- Bandfield, J.L., Ghent, R.R., Vasavada, A.R., Paige, D.A., Lawrence, S.J., Robinson, M.S., 2011. Lunar surface rock abundance and regolith fines temperatures derived from LRO diviner radiometer data. *J. Geophys. Res.* 116, E00H02. doi:10.1029/2011JE003866.
- Bandfield, J.L., Song, E., Hayne, P.O., Brand, B.D., Ghent, R.R., Vasavada, A.R., Paige, D.A., 2014. Lunar cold spots: granular flow features and extensive insulating materials surrounding young craters. *Icarus* 231, 221–231.
- Bandfield, J.L., Hayne, P.O., Williams, J.-P., Greenhagen, B.T., Paige, D.A., 2015. Lunar surface roughness derived from LRO diviner radiometer observations. *Icarus* 248, 357–372.
- Bandfield, J.L., Cahill, J.T.S., Carter, L.M., Neish, C.D., Patterson, G.W., Williams, J.-P., Paige, D.A., 2016. Distal ejecta from lunar impacts: extensive regions of rocky deposits. *Icarus* submitted.
- Basilevsky, A.T., Head, J.W., Horz, F., 2013. Survival times of meter-sized boulders on the surface of the Moon. *Planet. Space Sci.* 89, 118–126.
- Blewett, D.T., Hawke, B.R., Lucey, P.G., Taylor, G.J., 1995. Remote sensing and geological studies of the Schiller–Schickard region of the Moon. *J. Geophys. Res.* 100, 16959–16977.
- Cahill, J.S.T., Patterson, G.W., Turtle, E.P., Bussey, D.B.J., the Mini-RF Team, 2011. An analysis of orientale basin: integration of Mini-RF radar and optical mapping products. *Lunar Planet. Sci. Conf.*, 42nd abstract 2134.
- Cahill, J.S.T., Thomson, B.J., Patterson, G.W., Bussey, D.B.J., Neish, C.D., Lopez, N.R., Turner, F.S., Aldridge, T., McAdam, M., Meyer, H.M., Raney, R.K., Carter, L.M., Spudis, P.D., Hiesinger, H., Pasckert, J.H., 2014. The miniature radio frequency instrument's (Mini-RF) global observations of Earth's Moon. *Icarus* 243, 173–190.
- Campbell, B.A., Bell III, J.F., Zisk, S.H., Hawke, B.R., Horton, K.A., 1992. A high-resolution radar and CCD imaging study of crater rays in mare serenitatis and mare nectaris. In: *Lunar and Planetary Science Conference Proceedings*, vol. 22. Lunar and Planetary Institute, Houston, pp. 259–274.
- Campbell, B.A., Hawke, B.R., 2005. Radar mapping of lunar cryptomaria east of orientale basin. *J. Geophys. Res.* 110, E09002. doi:10.1029/2005JE002425.
- Chin, G., Brylow, S., Foote, M., Garvin, J., Kasper, J., Keller, J., Litvak, M., Mitrofanov, I., Paige, D., Raney, K., Robinson, M., Sanin, A., Smith, D., Spence, H., Spudis, P., Stern, S.A., Zuber, M., 2007. Lunar reconnaissance orbiter overview: the instrument suite and mission. *Space Sci. Rev.* 129, 391–419. doi:10.1007/s11214-007-9153-y.
- Conel, J.E., 1996. Infrared emissivities of silicates: experimental results and a cloudy atmosphere model of spectral emission from condensed particulate mediums. *J. Geophys. Res.* 74, 1614–1634.
- Cremers, C.J., Birkebak, R.C., 1971. Thermal conductivity of fines from apollo 12. In: *Proc. Lunar Sci. Conf.*, 2nd, pp. 2311–2315.
- Drozd, R.J., Hohenberg, C.M., Morgan, C.J., Podosek, F.A., Wroe, M.L., 1977. Cosmic-ray exposure history at taurus-littrow. In: *Proc. Lunar Sci. Conf.*, pp. 3027–3043.
- Dundas, C.M., McEwen, A.S., 2007. Rays and secondary craters of tycho. *Icarus* 186, 31–40.
- Eberhardt, P., Geiss, J., Grögler, N., Stettler, A., 1973. How old is the crater copernicus? *Moon* 8, 104–114.
- Fassett, C.I., Head, J.W., Smith, D.E., Zuber, M.T., Neumann, G.A., 2011. Thickness of proximal ejecta from the orientale basin from lunar orbiter laser altimeter (LOLA) data: implications for multi-ring basin formation. *Geophys. Res. Lett.* 38, L17201. doi:10.1029/2011GL048502.
- Gaddis, L.R., Pieters, C.M., Ray Hawke, B., 1985. Remote sensing of lunar pyroclastic mantling deposits. *Icarus* 61, 461–489.
- Gaddis, L.R., Staid, M.I., Tyburczy, J.A., Hawke, B.R., Petro, N.E., 2003. Compositional analyses of lunar pyroclastic deposits. *Icarus* 161, 262–280. doi:10.1016/S0019-1035(02)00036-2.
- Ghent, R.R., Leverington, D.W., Campbell, B.A., Hawke, B.R., Campbell, D.B., 2005. Earth-based observations of radar-dark crater haloes on the Moon: implications for regolith properties. *J. Geophys. Res.* 110, E02005. doi:10.1029/2004JE002366.
- Ghent, R.R., Campbell, B.A., Hawke, B.R., Campbell, D.B., 2008. Earth-based radar data reveal extended deposits of the Moon's orientale basin. *Geology* 36, 343–346. doi:10.1130/G24325A.1.
- Ghent, R.R., Hayne, P.O., Bandfield, J.L., Campbell, B.A., Allen, C.C., Carter, L.M., Paige, D.A., 2014. Constraints on the recent rate of lunar ejecta breakdown and implications for crater ages. *Geology* 42, 1059–1062.
- Ghent, R.R., Carter, L.M., Bandfield, J.L., Tai Udrovicic, C.J., Campbell, B.A., 2016. Lunar crater ejecta: physical properties revealed by radar and thermal infrared observations. *Icarus* 273, 182–195.
- Glotch, T.D., Lucey, P.G., Bandfield, J.L., Greenhagen, B.T., Thomas, I.R., Elphic, R.C., Bowles, N., Wyatt, M.B., Allen, C.C., Donaldson Hanna, K.L., Paige, D.A., 2010. Highly silicic compositions on the Moon. *Science* 329, 1510. doi:10.1126/science.1192148.
- Glotch, T.D., Hagerty, J.J., Lucey, P.G., Hawke, B.R., Giguere, T.A., Arnold, J.A., Williams, J.-P., Jolliff, B.L., Paige, D.A., 2011. The mairan domes: silicic volcanic constructs on the Moon. *Geophys. Res. Lett.* 38, L21204. doi:10.1029/2011GL049548.
- Greeley, R., Kadel, S.D., Williams, D.A., Gaddis, L.R., Head, J.W., McEwen, A.S., Murchie, S.L., Nagel, E., Neukum, G., Pieters, C.M., Sunshine, J.M., Wagner, R., Belton, M.J.S., 1993. Galileo imaging observations of lunar maria and related deposits. *J. Geophys. Res.* 98, 17183–17205.
- Greenhagen, B.T., 2009. Thermal Emission Remote Sensing of the Moon: Design and Development of Diviner Lunar Radiometer Compositional Capabilities. Ph. D. Thesis. University of California, Los Angeles.
- Greenhagen, B.T., Lucey, P.G., Wyatt, M.B., Glotch, T.D., Allen, C.C., Arnold, J.A., Bandfield, J.L., Bowles, N., Donaldson Hanna, K.L., Hayne, P.O., Song, E., Thomas, I.R., Paige, D.A., 2010. Global silicate mineralogy of the Moon from the diviner lunar radiometer. *Science* 329, 1507. doi:10.1126/science.1192196.
- Greenhagen, B.T., Neisch, C.D., Williams, J.-P., Petro, N.E., Hayne, P.O., Bandfield, J.L., 2016. Tsolkovskiy Crater: evaluating its enigmatic, fresh appearance. *Icarus* 273, 237–247.
- Grier, J., McEwen, A., Lucey, P., Milazzo, M., Strom, R., 2001. Optical maturity of ejecta from large rayed lunar craters. *J. Geophys. Res.* 106, 32,847–32,862.
- Gustafson, J.O., Bell, J.F., Gaddis, L.R., Hawke, B.R., Giguere, T.A., 2012. Characterization of previously unidentified lunar pyroclastic deposits using lunar reconnaissance orbiter camera data. *J. Geophys. Res.* 117. doi:10.1029/2011JE003893.
- Hayne, P.O., Ghent, R.R., Bandfield, J.L., Vasavada, A.R., Sielger, M.A., Greenhagen, B.T., Williams, J.-P., Paige, D.A., 2013. Formation and evolution of the Moon's upper regolith: constraints from diviner thermal measurements. *Lunar Planet. Sci. Conf.*, 44th abstract 3003.
- Hawke, B.R., MacLaskey, D., McCord, T.B., 1979. Multispectral Imaging of Lunar Crater Deposits, LPI Contribution, vol. 394. Lunar and Planet. Inst., Houston, Tex, pp. 50–52.
- Hawke, B.R., Peterson, C.A., Lucey, P.G., Taylor, G.J., Blewett, D.T., Campbell, B.A., Coombs, C.R., Spudis, P.D., 1993. Remote sensing studies of the terrain northwest of humonun basin. *Geophys. Res. Lett.* 20, 419–422.
- Hawke, B.R., Blewett, D.T., Lucey, P.G., Smith, G.A., Bell III, J.F., Campbell, B.A., Robinson, M.S., 2004. The origin of lunar crater rays. *Icarus* 170, 1–16. doi:10.1016/j.icarus.2004.02.013.
- Head, J.W., 1974. Lunar dark-mantle deposits: possible clues to the distribution of early mare deposits. In: *Proc. Lunar Sci. Conf.*, 5th, pp. 207–222.
- Head, J.W., Wilson, L., 1992. Lunar mare volcanism: stratigraphy, eruption conditions, and the evolution of secondary crusts. *Geochim. Cosmochim. Acta* 56, 2155–2175.
- Hiesinger, H., van der Bogert, C.H., Pasckert, J.H., Funcke, L., Giacomini, L., Ostrach, L.R., Robinson, M.S., 2012. How old are young lunar craters? *J. Geophys. Res.* 117, E00H10. doi:10.1029/2011JE003935.
- Hirata, N., Nakamura, A.M., Saiki, K., 2004. Ejecta and secondary crater distributions of tycho crater: effects of an oblique impact. *Lunar Planet. Sci. Conf.*, 35th abstract 1587.
- Horz, F., Schneider, E., Gault, D.E., Hartung, J.B., Brownlee, D.E., 1975. Catastrophic rupture of lunar rocks: a monte-carlo simulation. *The Moon* 13, 235–238.
- Hurley, D.M., Sarantos, M., Grava, C., Williams, J.-P., Retherfor, K.D., Siegler, M.A., Greenhagen, B.T., Paige, D.A., 2015. An analytic function of lunar surface temperature for exospheric modeling. *Icarus* 255 159 – 163.
- Keihm, S.J., Langseth, M.G., 1973. Surface brightness temperatures at the apollo 17 heat flow site: thermal conductivity of the upper 15 cm of regolith. In: *Proc. Lunar Sci. Conf.*, 5th, pp. 2503–2513.
- Krüger, T., van der Bogert, C.H., Hiesinger, H., 2013. New high-resolution melt distribution map and topographic analysis of tycho crater. *Lunar Planet. Sci. Conf.*, 44th abstract 2152.
- Lawson, S.L., Jakosky, B.M., Park, H.-S., Mellon, M.T., 2000. Brightness temperatures of the lunar surface: calibration and global analysis of the clementine long-wave infrared camera data. *J. Geophys. Res.* 105, 4273–4290.
- Linsky, J., 1966. Models of the lunar surface including temperaturedependent thermal properties. *Icarus* 5, 606–634.
- Lucey, P.G., Blewett, D.T., Taylor, G.J., Hawke, B.R., 2000. Imaging of lunar surface maturity. *J. Geophys. Res.* 105 (E8), 20,377–20,386. doi:10.1029/1999JE001110.
- Malla, R.B., Brown, K.M., 2015. Determination of temperature variation on lunar surface and subsurface for habitat analysis and design. *Acta Astro* 107, 196–207.
- Mazarico, E., Rowlands, D.D., Neumann, G.A., Smith, D.E., Torrence, M.H., Lemoine, F.G., Zuber, M.T., 2011a. Orbital determination of the lunar reconnaissance orbiter. *J. Geod.* 86, 193–207.

- Mazarico, E., Neumann, G.A., Smith, D.E., Zuber, M.T., Torrence, M.H., 2011b. Illumination conditions of the lunar polar regions using LOLA topography. *Icarus* 211, 1066–1081.
- McGovern, J.A., Bussey, D.B., Greenhagen, B.T., Paige, D.A., Cahill, J.T., Spudis, P.D., 2013. Mapping and characterization of non-polar permanent shadows on the lunar surface. *Icarus* 223, 566–581.
- Morris, A.R., Head, J.W., Margot, J.-L., Campbell, D.B., 2000. Impact melt distribution and emplacement on Tycho: a new look at an old question. *Lunar Planet. Sci. Conf.*, 31st abstract 1828.
- Mottaghi, S., Benaroya, H., 2015. Design of a lunar surface structure. I: design configuration and thermal analysis. *J. Aerosp. Eng.* 28. doi:[10.1061/\(ASCE\)AS-1943-5525.0000382](https://doi.org/10.1061/(ASCE)AS-1943-5525.0000382).
- Mustard, J.F., Head, J.W., 1996. Buried stratigraphic relationships along the southwestern shores of oceanus Procellarum: implications for early lunar volcanism. *J. Geophys. Res.* 101, 18,913–18,925.
- Neish, C.D., Blewett, D.T., Harmon, J.K., Coman, E.I., Cahill, J.T.S., Ernst, C.M., 2013. A comparison of rayed craters on the Moon and Mercury. *J. Geophys. Res.* 118, 2247–2261. doi:[10.1002/jgre.20166](https://doi.org/10.1002/jgre.20166).
- Nozette, S., Spudis, P., Bussey, B., Jensen, R., Raney, K., Winters, H., Lichtenberg, C.L., Marinelli, W., Cruson, J., Gates, M., Robinson, M., 2010. The lunar reconnaissance orbiter miniature radio frequency (Mini-RF) technology demonstration. *Space Sci. Rev.* 150, 285–302.
- Paige, D.A., et al., 2010a. The lunar reconnaissance orbiter diviner lunar radiometer experiment. *Space Sci. Rev.* 150, 125–160.
- Paige, D.A., et al., 2010b. Diviner lunar radiometer observations of cold traps in the Moon's south polar region. *Science* 330, 479–482.
- Paige, D.A., Williams, J.-P., Sullivan, M.T., Greenhagen, B.T., 2011. LRO diviner lunar radiometer global mapping results and gridded data product. *Lunar Planet. Sci. Conf.*, 42nd Abstract 2544.
- Ruess, F., Schänzlin, J., Benaroya, H., 2006. Structural design of a lunar habitat. *J. Aerosp. Eng.* 3 (133), 133–157. doi:[10.1061/\(ASCE\)0893-1321\(2006\)19](https://doi.org/10.1061/(ASCE)0893-1321(2006)19).
- Schultz, P.H., Mendell, W., 1978. Orbital infrared observations of lunar craters and possible implications for impact ejecta emplacement. In: *Proc. Lunar Sci. Conf.*, 9, pp. 2857–2883.
- Scott, D.H., McCauley, J.F., West, M.N., 1977. Geologic map of the west side of the Moon USGS Map, I-1034.
- Siegler, M., Paige, D.A., Williams, J.-P., Bills, B., 2015. Evolution of lunar polar ice stability. *Icarus* 255, 78–87.
- Smith, D.E., et al., 2010. Initial observations from the lunar orbiter laser altimeter (LOLA). *Geophys. Res. Lett.* 37, L18204. doi:[10.1029/2010GL043751](https://doi.org/10.1029/2010GL043751).
- Spudis, P.D., Hawke, B.R., Lucey, P., 1984. Composition of orientale basin deposits and implications for the lunar basin-forming process. In: *Proc. Lunar Planet. Sci. Conf.*, 15th, Part 1, pp. C197–C210. *J. Geophys. Res.*, 89, suppl.
- Spudis, P.D., Martin, D.J.P., Kramer, G., 2014. Geology and composition of the orientale basin impact melt sheet. *J. Geophys. Res.* 119. doi:[10.1002/2013JE004521](https://doi.org/10.1002/2013JE004521).
- Stöffler, D., Ryder, G., 2001. Stratigraphy and isotope ages of lunar geologic units: chronological standard for the inner solar system. *Space Sci. Rev.* 96, 9–54. doi:[10.1023/A:1011937020193](https://doi.org/10.1023/A:1011937020193).
- Sullivan, M.T., Paige, D.A., Arvidson, R.E., Grayzeck, E. (2013). Lunar Reconnaissance Orbiter Diviner Lunar Radiometer Experiment: Reduced Data Record and Derived Products Software Interface Specification. Tech. Rep. Version 1.13, PDS Geosciences Node.
- Thompson, T.W., Masursky, H., W.Shorthill, R., Tyler, G.L., 1974. A comparison of infrared, radar, and geologic mapping of lunar craters. *Moon* 10, 87–117.
- Thompson, T.W., Pollack, J.B., Campbell, M.J., O'Leary, B.T., 1970. Radar maps of the Moon at 70 cm wavelength and their interpretation. *Radio Sci.* 5, 253–262.
- Tooley, C.R., Houghton, M.B., Saylor Jr., R.S., Peddie, C., Everett, D.F., Baker, C.L., Safdie, K.N., 2010. Lunar reconnaissance orbiter mission and spacecraft design. *Space Sci. Rev.* 150, 23–62. doi:[10.1007/s11214-009-9624-4](https://doi.org/10.1007/s11214-009-9624-4).
- Vasavada, A.R., Paige, D.A., Wood, S.E., 1999. Near-surface temperatures on Mercury and the Moon and the stability of polar ice deposits. *Icarus* 141, 179–193.
- Vasavada, A.R., Bandfield, J.L., Greenhagen, B.T., Hayne, P.O., Siegler, M.A., Williams, J.-P., Paige, D.A., 2012. Lunar equatorial surface temperatures and regolith properties from the diviner lunar radiometer experiment. *J. Geophys. Res.* 117, E00H18. doi:[10.1029/2011JE003987](https://doi.org/10.1029/2011JE003987).
- Vondrák, R., Keller, J., Chin, G., Garvin, J., 2010. Lunar reconnaissance orbiter (LRO): observations for lunar exploration and science. *Space Sci. Rev.* 150, 1–4.
- Weitz, C.A., Head III, J.W., Pieters, C.M., 1998. Lunar regional dark mantle deposits: geologic, multispectral, and modeling studies. *J. Geophys. Res.* 103, 22,725–22,759.
- Whitten, J., Head, J.W., Staid, M., Pieters, C.M., Mustard, J., Clark, R., Nettles, J., Klima, R.L., Taylor, L., 2011. Lunar mare deposits associated with the orientale impact basin: new insights into mineralogy, history, mode of emplacement and relation to orientale basin evolution from Moon mineralogy mapper (M3) data from Chandrayaan-1. *J. Geophys. Res.* 116, E00G09. doi:[10.1029/2010JE003736](https://doi.org/10.1029/2010JE003736).
- Whitten, J.L., Head, J.W., 2015. Lunar cryptomaria: physical characteristics, distribution, and implications for ancient volcanism. *Icarus* 247, 150–171.
- Wilhelms, D.E., 1987. The geologic history of the Moon. U.S. Geol. Surv. Prof. Pap. 1348, 302.
- Williams, J.-P., Petro, N.E., Greenhagen, B., Neish, C., 2013. Inferred age of mare fill in tsiolkovskiy crater: constraints on the preservation of exterior impact melt deposits. *Lunar Planet. Sci. Conf.*, 44th.
- Williams, J.-P., Sefton-Nash, E., Paige, D.A., 2016. The temperatures of giordano bruno crater observed by the diviner lunar radiometer experiment: application of an effective field of view model for a point-based data set. *Icarus* 273, 205–213.
- Yu, S., Fa, W., 2016. Thermal conductivity of surficial lunar regolith estimated from lunar reconnaissance orbiter diviner radiometer data. *Planet. Space Sci.* 124, 48–61.
- Zisk, S.H., Pettengill, G.H., Catuna, G.W., 1974. High-resolution radar maps of the lunar surface at 3.8 cm wavelength. *Moon* 10, 17–50. doi:[10.1007/BF00562017](https://doi.org/10.1007/BF00562017).